Stable emission and excitation of the nitrogen-vacancy centre for quantum communication

THESIS

submitted in partial fulfillment of the
requirements for the degree of

MASTER OF SCIENCE
in
PHYSICS

Author :	Jacob J. W. Bakermans
Student ID :	s1169211
Supervisor :	Norbert Kalb, MSc.
	Dr. Andreas Reiserer
	Prof. dr. ir. Ronald Hanson
2^{nd} corrector :	Prof. dr. ir. Tjerk H. Oosterkamp

Leiden, The Netherlands, August 22, 2016

Stable emission and excitation of the nitrogen-vacancy centre for quantum communication

Jacob J. W. Bakermans

Huygens-Kamerlingh Onnes Laboratory, Leiden University
P.O. Box 9500, 2300 RA Leiden, The Netherlands

August 22, 2016

Abstract

In a quantum network, interconnected nodes use shared entangled states as a resource for communication. The nitrogen-vacancy (NV) centre in diamond is a promising candidate for the realization of a such a node. It provides a solid state qubit that can be initialized and read out optically and manipulated via microwave pulses. However, for any practical implementation, control mechanisms that maintain the resonance of the excitation and emission frequencies need to be in place. Additionally, to guarantee phase stability as required for long distance entanglement, it is necessary to realize a frequency stabilized excitation laser.
We demonstrate an autonomous routine for the optimization of excitation and emission frequencies, that recovers resonance conditions automatically when sudden jumps in the emission frequencies occur. Furthermore, an optical setup for the stabilization of excitation frequencies in a Pound-Drever-Hall scheme is presented. An upper bound on the excitation linewidth of 1.7 kHz is measured, yielding a phase deviation lower than 5° over a distance of 1 km. These developments will be essential in the development of a stand-alone quantum node involving the NV centre, on the road to a global quantum internet.

Contents

Chapter 1

Introduction

Quantum information science promises a range of new applications that are not possible with current-day technology, including simulation of quantum systems [1][2], quantum computation [3], secure communication [4], and high precision measurements [5]. In the implementation of each of those, quantum networks will play an important role [6][7]. In such a network, quantum nodes process and store quantum information, while quantum channels transport information between nodes. Such quantum channels are obtained by establishing entanglement between nodes. Entanglement can transport quantum information between nodes [8] via teleportation [9].
The nitrogen-vacancy (NV) centre in diamond is a promising candidate for the node in the quantum network [10]. Its spin state is used as a solid state qubit [11], which can be initialized and read out optically at cryogenic temperatures [12] and manipulated with microwave pulses. Moreover, the nuclear spin of ^{13}C isotopes in the surrounding carbon lattice can be controlled via the NV centre spin [13]. Since these nuclear spins can be isolated from their environment very well [14], they can be used as quantum memories. Entanglement of NV centres separated by more than 1 km has already been achieved [15]; the nuclear spins as quantum memories open the door to more advanced protocols, like entanglement purification [16][17] or entanglement swapping in a quantum repeater [18][19], which are crucial for truly long distance entanglement in an global quantum internet.
However, with the increase of experimental complexity, an increase in experimental control is required. Firstly, in order to generate entangled photons efficiently, several laser frequencies need to be adjusted continuously to stay on resonance with the optical transitions of the NV centre,

which display seemingly unpredictable jumps due to fluctuations in the local charge environment. Secondly, to guarantee a long-distance entangled state with known phase, the frequency of the laser that excites the NV centre needs to be stable on the time scale of the generation of entanglement [15]. Such a stable pair of lasers would therefore be an essential part of any long distance entanglement scheme with NV centres.
In this thesis, stabilization and automatic optimization of excitation and emission frequencies for long-distance entanglement with NV centres is presented. Chapter 2 demonstrates an autonomous control system that optimizes the excitation and emission frequency of three different optical transitions of the NV centre. In Chapter 3, a setup that locks a laser to a stable optical resonator, thus creating a frequency stabilized laser with a narrow linewidth, is presented, characterized, and evaluated. The questions that need to be answered are the following: what are the characteristics of the jumps in the emission frequencies of the NV, and can we compensate for them without human intervention? What is the linewidth of the stabilized laser, and will this be sufficient for long-distance entanglement experiments with the NV centre?

Chapter 2

Autonomous excitation frequency optimization

2.1 Theory and Motivation

2.1.1 The nitrogen-vacancy centre

The nitrogen-vacancy (NV) centre is a colour-centre in diamond that occurs naturally. It consists of a vacant lattice site next to a nitrogen atom replacing a carbon atom. The neutral charge state (NV^0) hosts 5 electrons, but it can capture an additional electron to arrive in the stable negatively charged state (NV^-) with a spin triplet ground state ($S = 1$) [20].
The NV^- charge state has our main interest as spin qubit. During experiments, the irradiation of the NV with several sources of laser light can induce a transition to the NV^0 state. It is possible to recover the negatively charged state by high power irradiation at a short wavelength, but this excites impurities in the neighbourhood of the NV as well, changing the surrounding charge distribution and thereby causing spectral shifts [21]. The spectral stability of the NV^- state is strongly increased under resonant excitation of NV^0 with low powers [22]. For this purpose, a yellow laser at 575 nm (the *charge repump* laser) is used [23].

2.1.2 Spin control

A simplified energy diagram with only the most relevant transitions in the NV^- charge state is drawn in Figure 2.1 [24]. The spin triplet ground state is split by 2.87 GHz into a $m_s = 0$ and $m_s = \pm 1$ state via the zero field

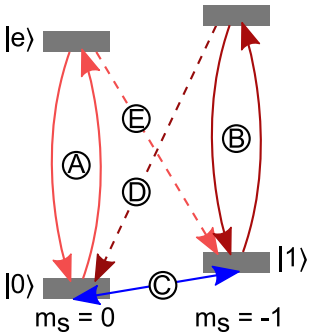

Figure 2.1: *Simplified energy diagram of the NV centre in diamond with the most relevant transitions. Quantum states $|0\rangle$, $|1\rangle$, and $|e\rangle$ can be assigned to the energy levels as shown.*

splitting, and an external magnetic field separates the $m_s = 1$ and $m_s = -1$ states. By assigning qubit states $|0\rangle$ to $m_s = 0$ and $|1\rangle$ to $m_s = -1$, the NV centre spin qubit is defined. Among the features that make the NV an attractive candidate for the quantum node is the fact that it can be initialized and read out optically [12]. At low temperature (T = 4K), it is possible to excite the qubit states $|0\rangle$ and $|1\rangle$ via spin-selective optical transitions (A and B in in Figure 2.1, respectively). Therefore, one can initialize the NV in state $|0\rangle$ by irradiating it with a laser resonant with transition B and the equivalent transition for $m_s = +1$ (the *spin repump* laser). If it is in $|0\rangle$, it will stay there, since the laser is off resonance with its excitation; if it is in $|1\rangle$, it will cycle transition B until a spin flip occurs (transition D). Similarly, the NV spin state is read out in a single shot by irradiating it with a laser resonant with transition A (the *readout laser*). If it is in $|0\rangle$, it will cycle transition A while emitting photons (*bright state*); if it is in $|1\rangle$, it will not fluoresce since the laser is not resonant with its transition (*dark state*). Transition E limits the read-out fidelity of state $|0\rangle$, but has a low probability [25].
Apart from the optical control, the state of the NV centre can be manipulated with microwave pulses that are applied via golden strip lines fabricated on the sample. Microwave pulses allow for universal control over the qubit state [26].

2.1.3 Motivation

To establish remote entanglement between distant NV centers, it is crucial that the emission from transition A of the NV center is on resonance with its excitation (see also Section 3.1.1). Before an experiment can start,

is is necessary to verify resonance. If no resonance condition is fulfilled the experiment is just idle and does not take any data. Therefore, to run the experiment efficiently, one should actively optimize the lasers and NV emission to make sure all three lasers involved are resonant with their respective optical transitions simultaneously. Each optical transition has a specific syndrome with which one can identify whether it is off resonance or not. If the charge repump laser is off-resonance, the NV will get stuck in its neutral charge state, and it will be impossible to obtain any photons from the fluorescent NV^- transitions. Likewise, an off-resonant spin repump laser will result in imperfect initialization. If the readout laser is not resonant with the excitation of $|0\rangle$, it will be difficult to achieve high readout fidelity. The frequencies corresponding to these optical transitions are not constant. The ongoing laser irradiation induces changes in the charge environment of the NV that inhomogeneously broaden its spectrum. Therefore a control mechanism is needed that continuously monitors spectral change and adjusts the frequencies of lasers and emission accordingly.

2.2 Methods

2.2.1 PID

In the simplest case without any frequency jumps, a proportional – integral – derivative (PID) controller [27] is sufficient to keep all frequencies on resonance. The goal of a PID controller is to keep a value, the *process variable*, as close as possible to an ideal value, the *set point*, by adjusting a parameter that can be controlled, the *control variable*. For this purpose, the control variable $u(t)$ is updated based on the *error signal*, the difference between the current value of the process variable and the set point. The updated $u(t)$ reads

$$u(t) = Pe(t) + I\int_0^t e(\tau)d\tau + D\frac{de(t)}{dt} \tag{2.1}$$

where $e(t)$ is the error signal, and P, I, and D parameters that determine the behaviour of the PID loop. P is the gain of the proportional part of the feedback. The proportional term pulls the process variable to the set point by changing the control variable proportionally to the current error. In the integral part, with I the integral gain, previous error values are taken into account as well to be able to correct for drifts on longer time scales. The differential gain D controls the differential part of the PID loop, that allows

for faster reaction to transient disturbance by using the rate of change of the error signal to predict future errors.

2.2.2 Charge-resonance check

The PID controller needs to be supplied with an error signal, and any form of automated optimizer will need a signal to optimize. The required data is provided by ongoing charge resonance (CR) checks. A fast programmable control unit, Adwin Pro II by Jäger GmbH, executes a CR check between executions of single-shot measurements (rate ~ 1 ms). A CR check consists of two stages: a modulation phase and a measurement phase. In the modulation phase, the frequency of the read-out transition is swept while measuring photon counts. The difference between the starting frequency and the frequency that produces the highest number of photons serves as an error signal for the PID loop that tries to keep the read-out transition on resonance. During the measurement phase following the modulation phase, the frequency is kept constant and photons are collected for a somewhat longer time (tens of microseconds). If the number of detected photons exceeds a certain threshold, the charge state is assumed to be NV^-; if not, the neutral charge state is detected and charge rempumping is necessary. In the first case, the counts are compared to another threshold to determine whether all resonance conditions are fulfilled to start a measurement. If the neutral charge state is detected, the same procedure (modulation and measurement) is carried out with the charge repump laser. The counts during the measurement phase can be made available to automated optimizers, that are used if the level of fluorescence is too low for the PID to work effectively.

2.2.3 Automated optimizers

The PIDs work well to compensate for gradual changes of resonance frequencies. However, after a sudden frequency jump has occurred, the counts during the modulation phase of the CR check are too low to obtain a useful error signal for the PIDs. To recover the resonance, a slow, long range frequency scan is carried out to maximize the counts during the measurement phase of the CR check (an *optimization* cycle). If necessary, the frequency sweep is repeated until the counts are high enough for the PIDs to take over again. For the charge repump transition and the spin repump transition, the corresponding laser frequency is adjusted by changing the current on the laser diode. In the case of the readout transi-

tion, the laser frequency is fixed (which is necessary for the entanglement protocol of Section 3.1.1) and the electric field at the NV centre is adjusted by changing the voltage of proximal DC electrodes.

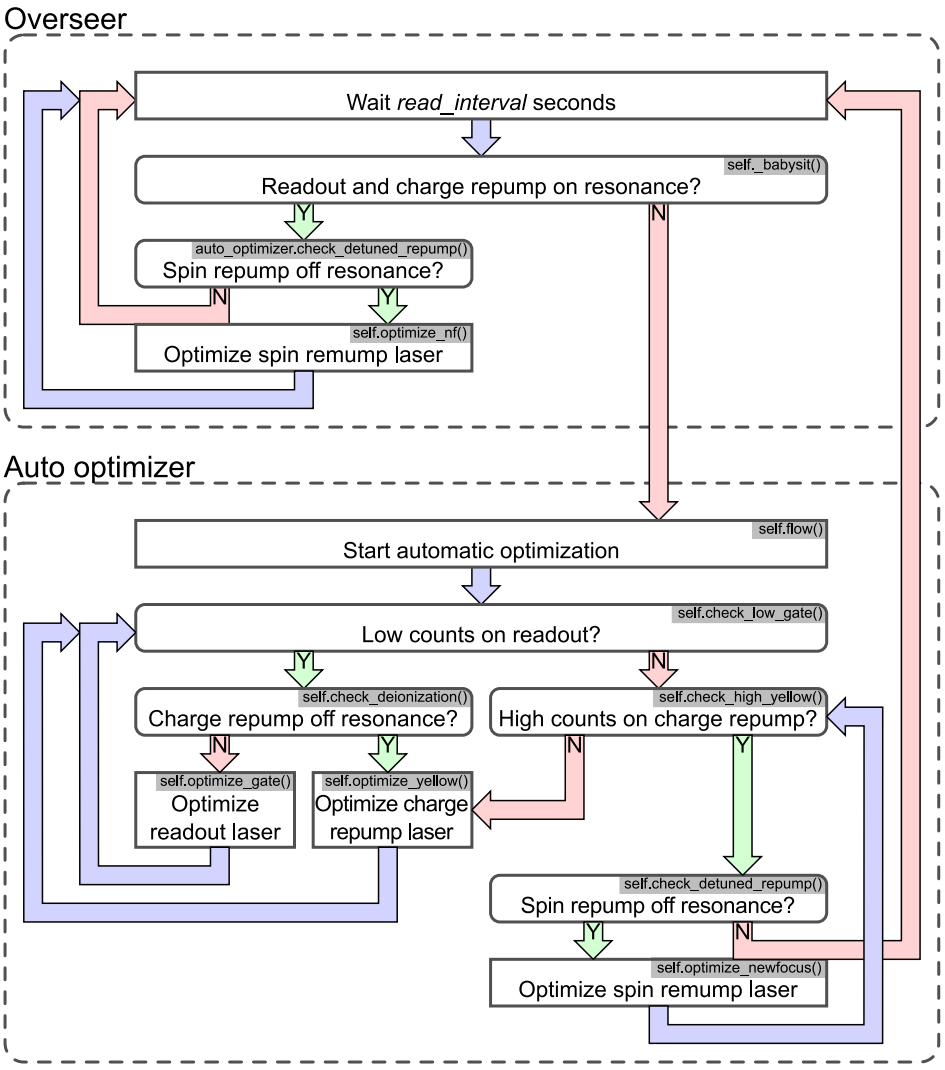

Figure 2.2: *Flowchart of operation when running the autonomous monitor-and-solve routine (babysitter). The objects involved, the overseer and the auto_optimizer, are separated by dashed lines. Conditions are drawn with rounded corners, with outcomes in green (Yes) and red (No), while actions have straight corners. For easy reference, the function name in the source code is provided in gray bars.*

Here, an in-depth explanation of the procedure that was implemented for automatic optimization is provided. All code is available under `https`:

//github.com/teamdiamond. The automatic optimization is governed by two objects that operate in *QT lab*, a heavily used command line tool that was developed at the Quantum Transport group of the TU Delft. The *overseer* is in charge of managing the available control mechanisms: the PIDs can be enabled or disabled, individual optimizers can be activated, and it can start and stop the autonomous monitor-and-solve routine (the *babysitter*). The *auto_optimizer* has functions for detecting and optimizing optical transitions, and generally comes into play when something is wrong. It is advantageous to take the interplay of different resonances into account. For example, optimizing the readout transition is irrelevant when the charge repump laser is off resonance - no counts will be detected as long as the charge state is NV^0. Therefore, the optimization functions of the auto_optimizer take the charge state into account to determine what transitions needs to be optimized. The interaction between the overseer, responsible for global control and monitoring, and the auto_optimizer, responsible for recovering resonances after a frequency jump, while running the babysitter is drawn schematically in Figure 2.2.
The performance of the overseer and auto_optimizer depends strongly on its parameters. An overview of all parameters is provided in Table A.1 in Appendix A.1.

2.3 Results

With the babysitter activated, it is possible to run an experiment that is demanding on the NV centre (i.e., it involves a lot of laser and microwave pulses) for hours without any human intervention. Although frequency jumps occur regularly, the automated optimizers are able to find back the resonances without exception. During these experiments, the frequency is logged when all lasers are on resonance in order to characterize the frequency jumps. The result of these frequency measurements are presented here. Since the behaviour of the transition frequencies strongly depends on the NV, the results are shown separately for the NV centre in the Low Temperature setup 3 (LT3) and for the NV centre in the Low Temperature setup 4 (LT4).

2.3.1 LT3

The frequency of the charge repump laser and the voltage on the DC electrode, which determines the frequency of the readout transition, are measured during several experiments. By stitching the individual experimen-

tal runs together, a time trace of the evolution of the transition frequencies over more than thirty hours is obtained. In Figure 2.3, the voltage applied to the DC electrode while the readout transition is on resonance is shown. Figure 2.4 shows the frequency of the charge repump laser.

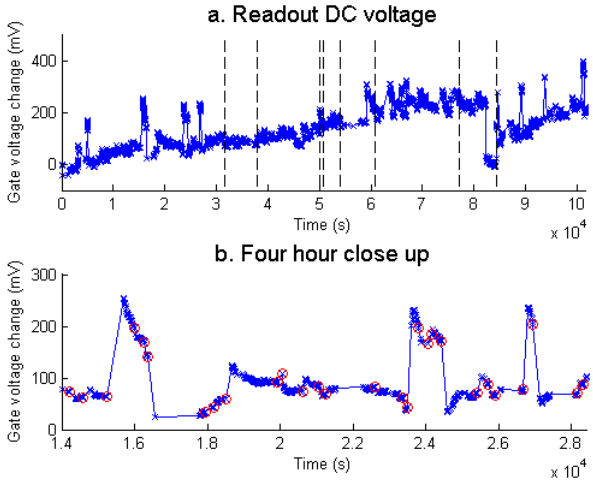

***Figure 2.3: a**. Evolution of the voltage on the DC electrode, which determines the frequency of the readout transition, during experiments over the course of close to thirty hours. The black dashed lines show where the time trace was stitched out of separate experiment runs. **b**. A four hour zoomed-in time window. Blue crosses mark frequency measurements, which are only carried out when all lasers are on resonance. Red circles indicate a frequency jump that was resolved by the automatic optimizer.*

From the data of Figure 2.3 and 2.4, the frequency difference of the jumps indicated with red circles are extracted. A jump is defined as an interval without frequency measurements (meaning at least one resonance was lost) of at least 3 times the median of time difference between data points. Since periods without frequency measurements can also occur for other reasons than frequency jumps, only events with a frequency difference larger than the median of frequency differences are confirmed as a frequency jump. It is verified by eye that these thresholds produce real jumps and filter out other events. The distribution of frequency jumps is shown in the histograms of Figure 2.5. Interestingly, there are secondary peaks in the histograms, somewhat separated from the central peak.

From a practical point of view, the most interesting property of the frequency jumps is their predictability. The efficiency of data acquisition in experiments could be strongly increased if one would be able to predict the

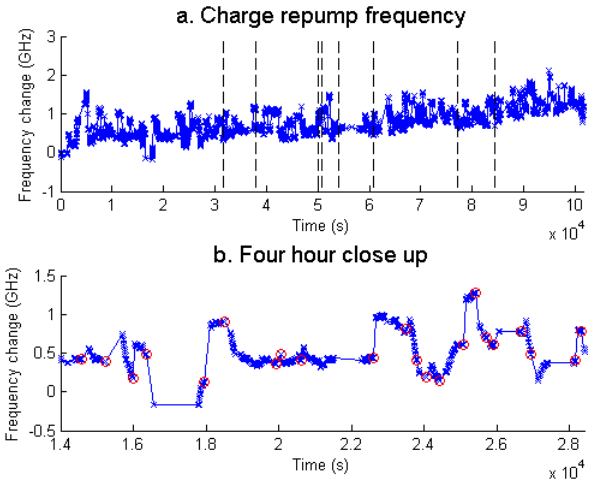

Figure 2.4: ***a****. Evolution of the frequency of the charge repump laser during experiments over the course of close to thirty hours. The black dashed lines show where the time trace was stitched out of separate experiment runs.* ***b****. A four hour zoomed-in time window. Blue crosses mark frequency measurements, which are only carried out when all lasers are on resonance. Red circles indicate a frequency jump that was resolved by the automatic optimizer.*

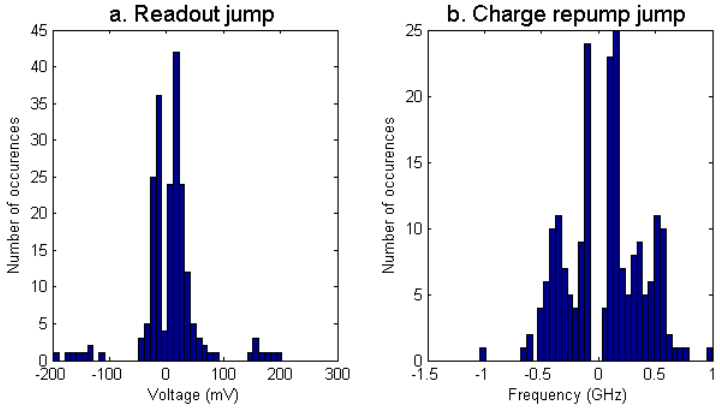

Figure 2.5: *Histograms of the frequency jumps in* ***a****. the readout transition and* ***b****. the charge repump transition.*

direction and amplitude of the frequency jump. Figure 2.4b shows some signs of predictability: judging by eye, the frequency alternates between a high and low value, suggesting that from above the average frequency, a jump will most likely go down, while from below the average frequency, a jump will most likely go up. To test this hypothesis, a heat map of the difference between the frequency at the moment of the jump against the

measured jump is constructed in Figure 2.6. In addition to characterizing

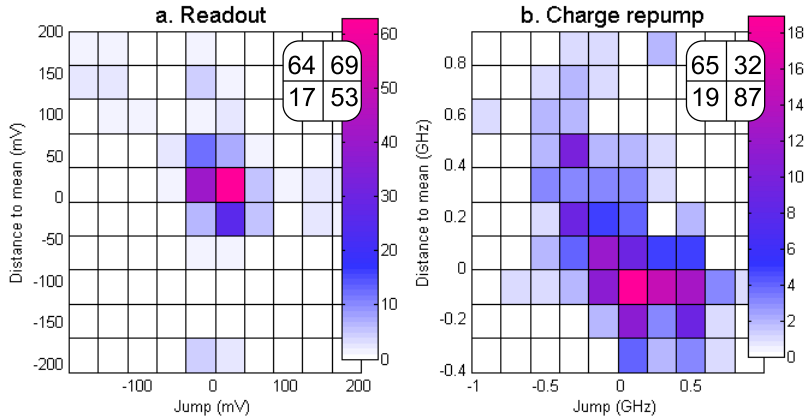

Figure 2.6: *Heatmap to investigate the relation between difference from the average frequency and the measured frequency jump. The average frequency is calculated from the last stitching point to the moment of the jump to simulate the available information in a real experiment. The inset tables indicate the number of jumps in the four quadrants.*

the frequency jumps that occur during the experiment, the data of Figure 2.3 and 2.4 also enable the evaluation of the performance of the automatic optimizer. In Figure 2.7, a histogram of the time it takes for the automatic optimizer to recover resonance after a frequency jump is plotted. From this cumulative density function, one can read off that 50 % of the frequency jumps has been resolved within 85 s, and 90 % within 5 minutes.

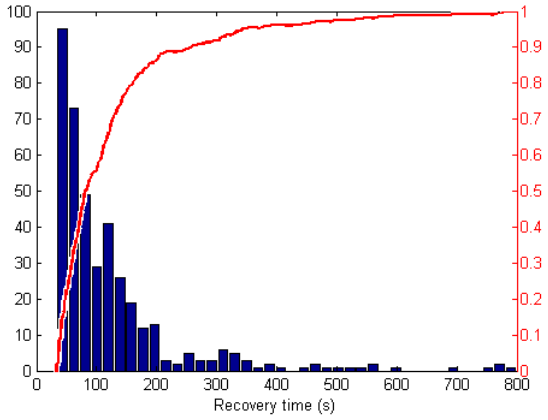

Figure 2.7: *Histogram of the time it takes the automatic optimizer to get all lasers back to resonance for all frequency jumps. The cumulative density function is plotted in red.*

2.3.2 LT4

From experience, the frequency of the optical transitions of the NV in LT4 seems more stable than the NV in LT3. Figure 2.8 and 2.9 confirm the higher stability of this NV.

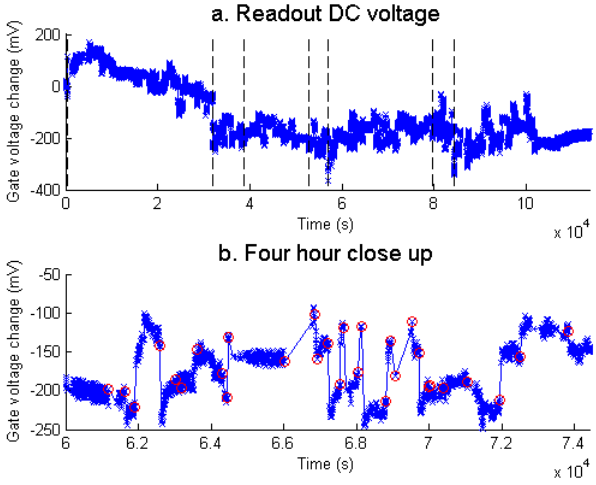

***Figure 2.8: a**. Evolution of the voltage on the DC electrode, which determines the frequency of the readout transition, during experiments over the course of close to thirty hours. The black dashed lines show where the time trace was stitched out of separate experiment runs. **b**. A four hour zoomed-in time window. Blue crosses mark frequency measurements, which are only carried out when all lasers are on resonance. Red circles indicate a frequency jump that was resolved by the automatic optimizer.*

The histograms of frequency jumps for the NV in LT4 are provided in Figure 2.10. Jumps are defined in the same way as in Section 2.3.1, except that the frequency difference of a jump needs to be at least twice the median to filter out more false positives. Again, the relative stability is confirmed when comparing Figure 2.10 to Figure 2.5.

Unsurprisingly, the frequency jumps of the NV in LT4 are resolved by the automatic optimizer more rapidly than in LT3. From Figure 2.11 it is concluded that 50 % of the frequency jumps has been resolved within 30 s, and 90 % within 2 minutes.

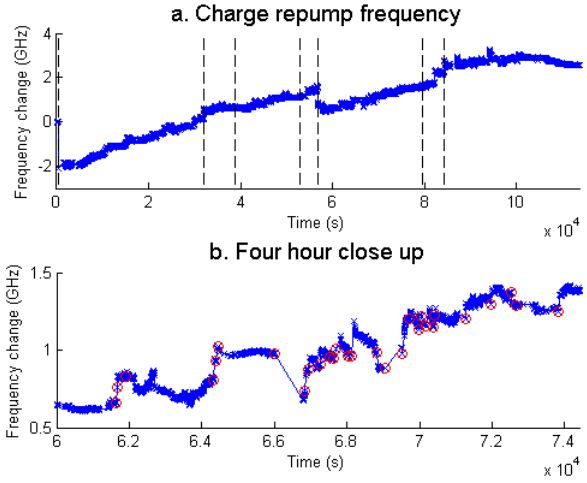

Figure 2.9: ***a****. Evolution of the frequency of the charge repump laser during experiments over the course of close to thirty hours. The black dashed lines show where the time trace was stitched out of separate experiment runs.* ***b****. A four hour zoomed-in time window. Blue crosses mark frequency measurements, which are only carried out when all lasers are on resonance. Red circles indicate a frequency jump that was resolved by the automatic optimizer.*

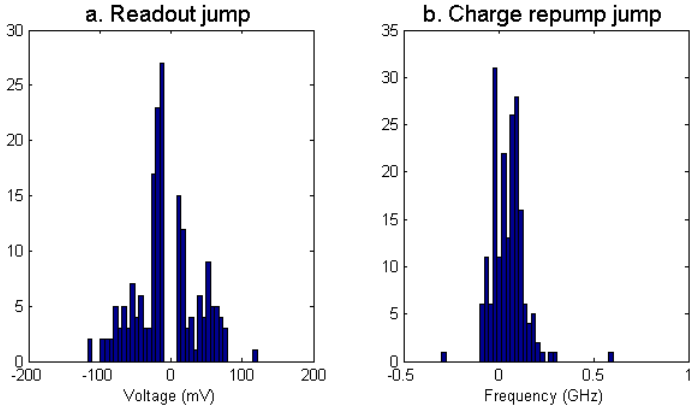

Figure 2.10: *Histograms of the frequency jumps in* ***a****. the readout transition and* ***b****. the charge repump transition.*

2.4 Discussion and Conclusion

A first conclusion concerns the performance of the babysitter, that monitors, detects, and resolves frequency jumps automatically. Frequency data has been recorded over many hours of experiments, during which the experimenter's task has been reduced from constantly watching and tuning

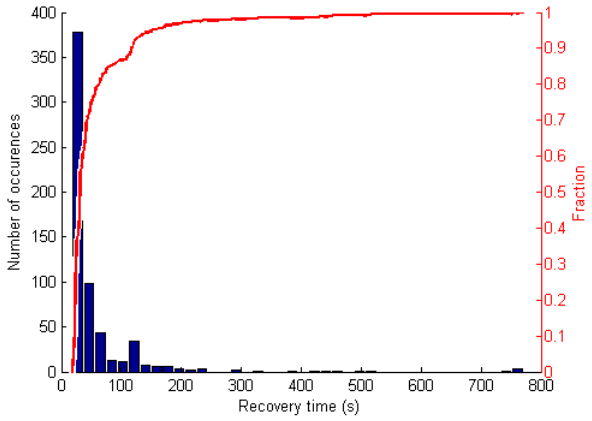

Figure 2.11: *Histogram of the time it takes the automatic optimizer to get all lasers back to resonance for all frequency jumps. The cumulative density function is plotted in red.*

the optical transitions to checking every once in a while whether other parameters of the experiment are still as expected. Excitation of each optical transition is optimized on a time scale of seconds to minutes, even if multiple transitions jump off resonance simultaneously, without human intervention. Clearly, data acquisition in a more time-efficient manner has been achieved. Not only can the experimenter focus on other things, but the babysitter also managed to increase the duty cycle of the experiment from 23 % to 28 % - it actually outperforms humans at preserving resonance. In future experiments, the babysitter will be a valuable addition to the experimental control toolbox.
A big difference in frequency stability is observed between the NV in the LT3 setup and the NV in the LT4 setup. In LT4, frequency jumps occur less often and have a smaller amplitude, which leads to faster recovery of resonance conditions. The reason for this difference in behaviour between NVs is most likely their environment, where charges may be excited or trapped, especially their distance to the surface. The NV in LT3 lies several micrometers closer to the diamond surface. For automation purposes, one needs to be able to decouple control from the specific properties of the emitter. Therefore, characterizing frequency jumps in order to identify underlying mechanisms is a sensible endeavour.
In the frequency jumps of the optical transitions of the NV in LT3, two effects seem to play a role. First, there is a long term drift in both frequencies, caused by many small jumps that make up the central peak of the jump frequency histograms of Figure 2.5. These drifts can be caused by

relatively fast (otherwise the PIDs can catch it) charge buildup far away from the NV centre. The second effect is a form of bistability: jumps with an amplitude over 100 mV or 0.5 GHz that can go both up and down, occurring less frequently, after which the frequency remains at the new level for a while. Both the time traces of Figure 2.3 and 2.4 and the histograms of Figure 2.5 support this observation of bistable behaviour. An explanation could be that a single charge trap near the NV centre is alternatively occupied or unoccupied. One should be aware that during optimization, the frequency might still drift, even more so if the optimization takes minutes. Therefore, it is very well possible that the distribution of jumps will change slightly if faster recovery is achieved. Characterizing frequency jumps will be an iterative process: every time increased optimization is implemented, a more realistic frequency jump distribution is obtained.
The greatest opportunity for improving the automatic recovery of optical transition resonance, thus decreasing experimental down time, would be predicting the direction and amplitude of a frequency jump. Ideally, whenever it is detected that one of the lasers is off resonance, an algorithm would evaluate previous frequency measurements and based on those predict the current frequency jump. For this purpose, a machine learning algorithm might be implemented [28]. The frequency measurements that have been carried out here, with the addition of frequency logging datasets acquired during ongoing measurements, will provide an extensive training set for a machine learning algorithm to learn the relevant frequency dynamics. These frequency dynamics are highly specific for each NV centre. An advantage of machine learning would be that it can adapt, just by evaluating frequency data, to any new NV centre.

Chapter 3

Laser stabilization

3.1 Theory and Motivation

3.1.1 Entanglement

We use the Barrett and Kok protocol to establish entanglement between NVs [29]. The following steps are executed at each node individually. First, the NV is initialized in the $|0\rangle$ state and a microwave $\pi/2$ pulse is applied, such that

$$|\Psi\rangle_{NV} = \frac{1}{\sqrt{2}}(|0\rangle + |1\rangle) \tag{3.1}$$

Then, an optical π pulse excites $|0\rangle$ to $|e\rangle$, and after waiting long enough to guarantee spontaneous emission, the state decays back to $|0\rangle$. The combined spin-photon state then reads

$$|\Psi\rangle = \frac{1}{\sqrt{2}}(|0\rangle_{NV}|1\rangle_{photon} + |1\rangle_{NV}|0\rangle_{photon}) \tag{3.2}$$

with the photonic Fock states $|n\rangle_{photon}$, where n is the number of photons. The occurrence of two-photon emission and off-resonant excitation decreases the fidelity of this state; the probability of both is simulated in Section A.2. In Equation 3.2, spin-photon entanglement has already been achieved, but the state $|1\rangle_{photon}$ is difficult to distinguish from the state $|0\rangle_{photon}$ in the case of high photon loss. Therefore a microwave π pulse is applied, flipping $|0\rangle_{NV}$ to $|1\rangle_{NV}$ and vice versa, followed by an optical π pulse. After spontaneous emission, switching to the more convenient photon time bin notation, the combined spin-photon state reads

$$|\Psi\rangle = \frac{1}{\sqrt{2}}(|1\rangle_{NV}|E\rangle_{photon} + |0\rangle_{NV}|L\rangle_{photon}) \tag{3.3}$$

where $|E\rangle_{photon}$ stands for a photon emitted after the first optical π pulse, or early time bin, and $|L\rangle_{photon}$ corresponds to a photon emitted after the second optical π pulse, or late time bin.
In order to establish entanglement between distant NV centres A and B, both are prepared in the state of Equation 3.3:

$$|\Psi\rangle_{AB} = \frac{1}{2}(|1\rangle_A|E\rangle_A|1\rangle_B|E\rangle_B + |1\rangle_A|E\rangle_A|0\rangle_B|L\rangle_B + |0\rangle_A|L\rangle_A|1\rangle_B|E\rangle_B + |0\rangle_A|L\rangle_A|0\rangle_B|L\rangle_B) \tag{3.4}$$

Any emitted photons are overlapped on a beamsplitter to erase 'which-path' information. If the detectors behind the beamsplitters now measure an early *and* a late photon, the state of Equation 3.4 collapses to

$$|\Psi\rangle_{AB} = \frac{1}{\sqrt{2}}(|1\rangle_A|E\rangle_A|0\rangle_B|L\rangle_B \pm |0\rangle_A|L\rangle_A|1\rangle_B|E\rangle_B) \tag{3.5}$$

Notice the $\pm$ sign, caused by the fact that reflection on the beamsplitter causes a π phase shift [30]. Equation 3.5 shows that as soon as an early photon and a late photon have been detected, the spins of the two NV centres have become entangled. The measurement of both photons guarantees that the spin states of NV centre A and B are entangled; there is no other way to detect an early and a late photon. We thus have *heralded* entanglement [31]. Leaving out the photon states, which have become irrelevant since the photons have been measured, we can write the combined state as the desired maximally entangled state

$$|\Psi^{\pm}\rangle_{AB} = \frac{1}{\sqrt{2}}(|1\rangle_A|0\rangle_B \pm |0\rangle_A|1\rangle_B) \tag{3.6}$$

Phase

In the derivation of Equation 3.6, some assumptions were made. First, it was assumed that the optical path from A to the beamsplitter (and therefore the phase picked up by photons from the side of A) is identical to the optical path from B to the beamsplitter. The protocol described above does not require this assumption. Instead, assume that a photon coming from A picks up a phase ϕ and a photon coming from B picks up a phase θ due to differences in the optical path. Equation 3.5 becomes

$$\begin{aligned}|\Psi\rangle_{AB} &= \frac{1}{\sqrt{2}}(e^{i\phi}|1\rangle_A|E\rangle_A e^{i\theta}|0\rangle_B|L\rangle_B \pm e^{i\phi}|0\rangle_A|L\rangle_A e^{i\theta}|1\rangle_B|E\rangle_B) \\ &= \frac{e^{i(\phi+\theta)}}{\sqrt{2}}(|1\rangle_A|E\rangle_A|0\rangle_B|L\rangle_B \pm |0\rangle_A|L\rangle_A|1\rangle_B|E\rangle_B)\end{aligned} \tag{3.7}$$

where the phase due to different optical paths has become a global phase. Other phase factors that were not included in the derivation of Equation 3.3 include the precession of the NV spin state due to the energy difference between $|0\rangle$ and $|1\rangle$, which is cancelled by the microwave π pulse, and the phase picked up during the time spent in the excited state $|e\rangle$, accounted for by post-selecting photons that were detected within a short time window or keeping the NV centres on resonance [31].
Another assumption that was made is that the same laser applies optical π pulses to both NVs. For NV centres separated by a large distance, this is not likely to be the case. When the $|0\rangle$ state is excited to $|e\rangle$, the phase of the laser is imprinted on the emitted photon. The state of a single NV centre-photon state of Equation 3.3 becomes

$$|\Psi\rangle = \frac{1}{\sqrt{2}}(e^{\phi_E}|1\rangle_{NV}|E\rangle_{photon} + e^{\phi_L}|0\rangle_{NV}|L\rangle_{photon}) \tag{3.8}$$

where ϕ_E is the phase of the laser at the moment of the first optical π pulse, and ϕ_L is the phase of the laser at the moment of the second optical π pulse. The entangled state in the case of a separate laser at each NV becomes

$$|\Psi\rangle_{AB} = \frac{1}{\sqrt{2}}(e^{i\phi_E}|1\rangle_A|E\rangle_A e^{i\theta_L}|0\rangle_B|L\rangle_B \pm e^{i\phi_L}|0\rangle_A|L\rangle_A e^{i\theta_E}|1\rangle_B|E\rangle_B) \tag{3.9}$$

where ϕ is the phase of the laser at A and θ is the phase of the laser at B at the moment of the optical π pulse. This time, the phase will only be a global phase if

$$e^{i\phi_E}e^{i\theta_L} = e^{i\phi_L}e^{i\theta_E} \Leftrightarrow \phi_E + \theta_L = \phi_L + \theta_E \Leftrightarrow \phi_L - \phi_E = \theta_L - \theta_E \tag{3.10}$$

If the NVs are excited with the same laser, the condition of Equation 3.10 would automatically be met. However, in the case of two different lasers, both lasers should have the exact same frequency between the two optical π pulses to guarantee an identical phase difference. Frequency-stabilized lasers will be necessary for long-distance quantum communication.

3.1.2 Pound-Drever-Hall feedback

A technique to stabilize the frequency of a laser is the Pound-Drever-Hall scheme [32]. In a Pound-Drever-Hall setup, the phase of the reflected beam from the cavity is utilized as an error signal. If the laser light is

on resonance with the cavity, the light wave exactly fits into the cavity, i.e. half the wavelength is the cavity length divided by an integer, or

$$\omega = \frac{nc}{2L}$$

where c is the speed of light, L is the length of the cavity, and n is integer. Near resonance, a linear relation exists between the phase of the reflected laser light and the frequency deviation. Clearly, the phase of the reflected light is a more sensible measure of frequency deviation than the intensity, since it is antisymmetric around resonance and it decouples frequency fluctuations from intensity fluctuation. The Pound-Drever-Hall scheme provides a way to measure this phase [33].
For this purpose, sidebands are added to the laser output, for example by periodically modulating the phase of the laser light with an electro-optic modulator (EOM). If the laser electric field before modulation is described by

$$E(t) \propto e^{i\omega t} \tag{3.11}$$

where ω is the laser frequency, the EOM will add a time dependent phase

$$E(t) \propto e^{i\omega t + i\beta \sin(\Omega t)} \tag{3.12}$$

with Ω the modulation frequency and β the modulation amplitude. For small β, Equation 3.12 can be rewritten as

$$E(t) \propto e^{i\omega t} + \frac{\beta}{2} e^{i(\omega+\Omega)t} - \frac{\beta}{2} e^{i(\omega-\Omega)t} \tag{3.13}$$

showing the sidebands at $\omega + \Omega$ and $\omega - \Omega$. After adding frequency sidebands, the laser light is guided into the cavity. As described before, at a frequency near resonance an additional phase is introduced. Since the sidebands are far away from resonance, only the central frequency is affected by the cavity. The field becomes

$$E(t) \propto e^{i(\omega t+\phi)} + \frac{\beta}{2} e^{i(\omega+\Omega)t} - \frac{\beta}{2} e^{i(\omega-\Omega)t} \tag{3.14}$$

After reflection off the cavity, the light is measured on a photodiode. A photodiode measures the intensity of the light and converts it to an electrical signal. The intensity is given by

$$I \propto |E|^2 \tag{3.15}$$

For the electric field of Equation 3.14, we find that the intensity shows a beat pattern at the frequency of modulation Ω:

$$\begin{aligned} I \propto & \left(e^{i(\omega t+\phi)} + \frac{\beta}{2} e^{i(\omega+\Omega)t} - \frac{\beta}{2} e^{i(\omega-\Omega)t} \right) \left(e^{-i(\omega t+\phi)} + \frac{\beta}{2} e^{-i(\omega+\Omega)t} - \frac{\beta}{2} e^{-i(\omega-\Omega)t} \right) \\ \propto & 1 + \beta \cos(\Omega t - \phi) - \beta \cos(\Omega t + \phi) - \frac{\beta^2}{2} \cos(2\Omega t) + \frac{\beta^2}{2} \end{aligned} \tag{3.16}$$

Discarding the terms of order β^2, because β was assumed to be small, the photodiode output voltage becomes

$$S_{PD} \propto 1 + \beta \cos(\phi - \Omega t) - \beta \cos(\phi + \Omega t) \tag{3.17}$$

Note that this signal contains the phase ϕ of the laser frequency introduced by the cavity, which is the quantity that we are after. Finally, the electrical signal is mixed with the original modulation signal. An electronic mixer produces the product of the inputs it receives. The output of the mixer is then

$$\begin{aligned} S_{mixer} & \propto \sin(\Omega t) \left(1 + \beta \cos(\phi - \Omega t) - \beta \cos(\phi + \Omega t)\right) \\ & \propto \sin(\Omega t) + \beta \sin(\phi) + \beta \sin(2\Omega t - \phi) - \beta \sin(-\phi) - \beta \sin(2\Omega t + \phi) \end{aligned} \tag{3.18}$$

The DC component of the mixer output is proportional to the sine of the phase and can be retrieved by low pass filtering the signal. In the Pound-Drever-Hall feedback setup, the feedback bandwidth is limited by how fast the laser frequency can be adapted. Since the modulation frequency Ω is too high for the laser to follow, only the DC component will be relevant for the feedback. Therefore the output of the mixer can directly serve as a phase measurement for the frequency stabilization in a Pound-Drever-Hall setup.

3.1.3 Motivation

As argued in Section 3.1.1, a frequency stabilized laser is necessary in order to create an entangled state with predictable phase with NV centres that are excited by different lasers. Between the optical π pulses, the excitation frequency should not only be stable, but actually be identical at both NV centres. The frequency of one laser needs to be distributed to the other to be able to compare frequencies [34], but transferring the signal induces a delay. Therefore, the required frequency stability is dictated by the distance between the two NV centres as well as the time between optical

π pulses. For a phase stability of $\Delta\phi$, the required frequency stability is given by

$$\Delta f = \frac{\Delta\phi}{T}, T = \Delta t_\pi + \Delta t_d \approx \Delta t_\pi + \frac{d \times n}{c} \tag{3.19}$$

with Δt_π the interval between optical π pulses and Δt_d the time delay due to distance, d the distance between the NVs, c the speed of light in vacuum and n the refractive index of the optical fibre. The required frequency stability is plotted against distance for different phase stabilities in Figure 3.1. Concretely, for a phase deviation of 1° over a distance of 10 km, in the protocol of Section 3.1.1 with 300 ns between optical π pulses, the frequency deviation can be no more than 55 Hz over a time of 50 µs.

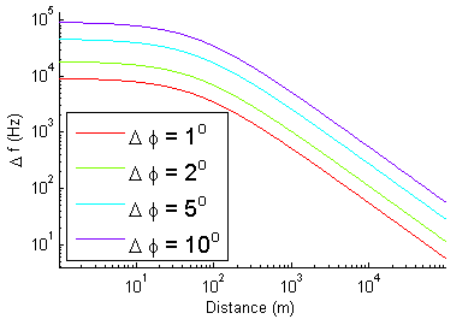

Figure 3.1: *Required frequency stability to obtain a certain phase stability in the protocol of Section 3.1.1 with* 300 ns *between optical π pulses, plotted against distance between the NVs.*

3.2 Methods

3.2.1 Setup

The setup that was implemented to stabilize (*lock*) a laser in a Pound-Drever-Hall scheme is shown schematically in Figure 3.2.

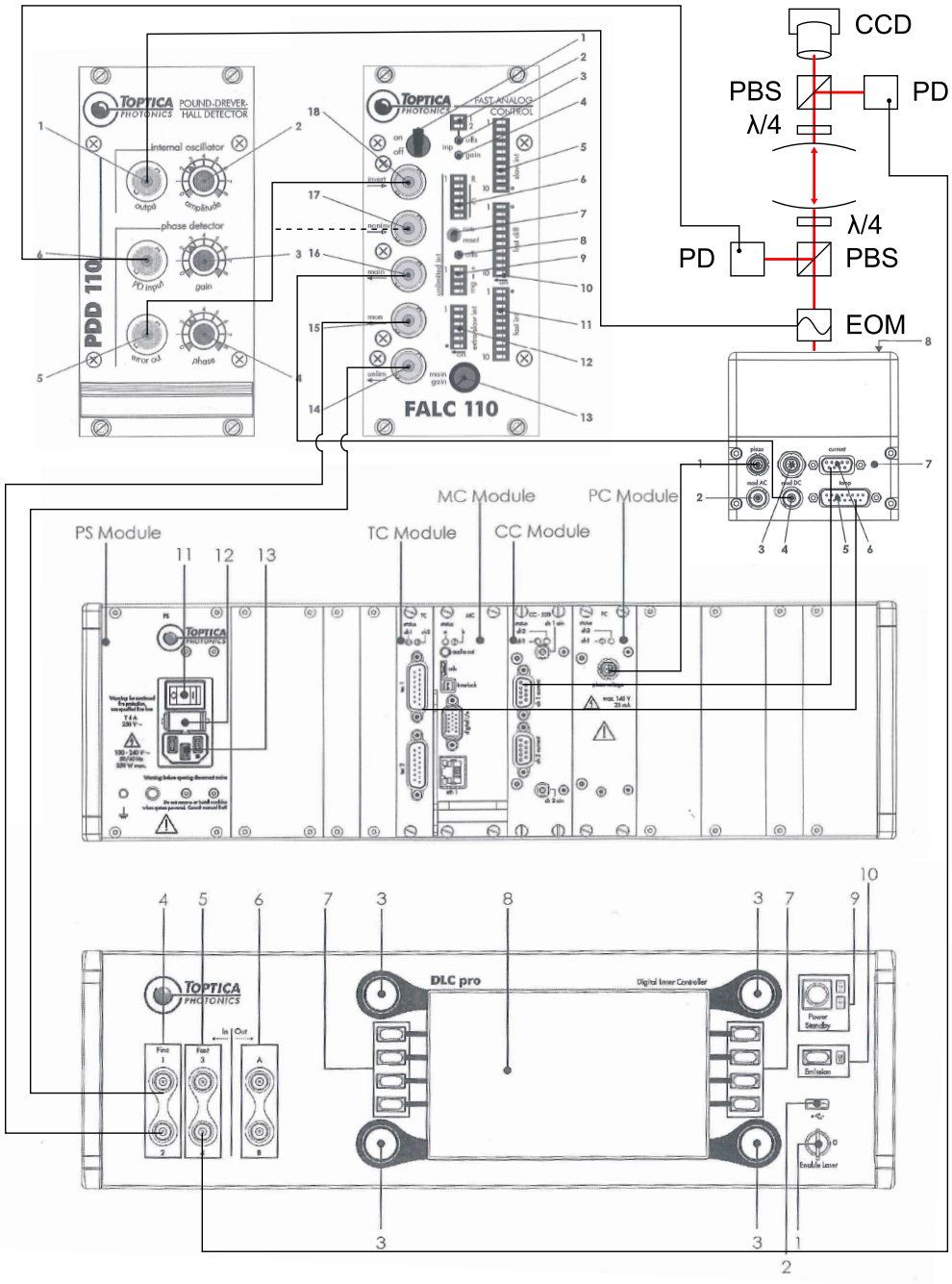

Figure 3.2: *Setup for PDH locking, with Toptica PDD 110 module, Toptica FALC 110, and Toptica DLC pro with laser head. See the the manual of the respective modules for further information. The (simplified) optical setup, containing all essential parts, consists of an electro-optical modulator (EOM), fibre beam splitters (FBS), photodiodes (PD), quarter wave plates ($\lambda/4$), a CCD camera (CCD), and the cavity.*

A Toptica grating stabilized diode DL Pro laser is locked to a in-house developed cavity. The cavity is about 10 cm long and made out of zerodur, a type of ultra low expansion glass that can reach the zero thermal expansion point around room temperature, with a mirror coating on both sides. To isolate the cavity from thermal and vibrational noise, it is mounted in a vacuum tube and placed in a box filled with isolation material, which is screwed to an actively vibration damped optical table. The PDH error signal is generated by a PDD 110 Pound Drever Hall detector module from Toptica. It contains a local oscillator at 20 MHz which supplies the modulation signal to the EOM (Equation 3.12). It has an input port for the intensity signal from the photodiode (PD) that measures the reflection off the cavity (Equation 3.16), which is mixed down with the local oscillator internally (Equation 3.18) and finally connected from an output port to the input of a Fast Analog Linewidth Control FALC 110 module from Toptica. The FALC module converts the PDH error signal to the actual current that is supplied to the laser diode via the DC modulation input port. The parameters of the PID control implemented by the FALC module can be adjusted via flip switches on the front. The overall gain of the feedback signal can be set from the FALC module as well. The output port on the FALC module labeled with *unlimited int* is connected to the Toptica digital laser controller DLC Pro, which in turn outputs a voltage to the piezo that controls the grating of the laser, in order to stabilize the laser against drifts on the time scale of seconds to hours. To monitor the locking performance and optimize the parameters that govern the behaviour of the feedback, it is useful to connect the monitor output of the FALC module to one of the input channels on the front of the DLC. The monitor output allows inspection of the feedback signal that is provided to the laser by the FALC module. By connecting a photodiode that measures transmission through the cavity to another input of the DLC, one can evaluate the relation between feedback output and locking performance. Finally, a CCD camera monitors the transmitted light from the cavity to distinguish which cavity mode is excited.

Optics

In order to achieve good coupling into the cavity mode, it is important to align the beam waist to the waist of the cavity mode. The waist of a Gaussian beam in free space is described by

$$w(z) = w_0\sqrt{1+\left(\frac{z}{z_R}\right)^2},\ z_R = \frac{\pi w_0^2}{\lambda} \tag{3.20}$$

where z is the position relative to the focus of the beam, w_0 is the waist at the focus, and λ is the wavelength. The lens of a fibre coupler is sufficient to couple the light emitted from an optical fibre into the cavity mode if it is placed in the appropriate position. In Figure 3.3, the waist of the image

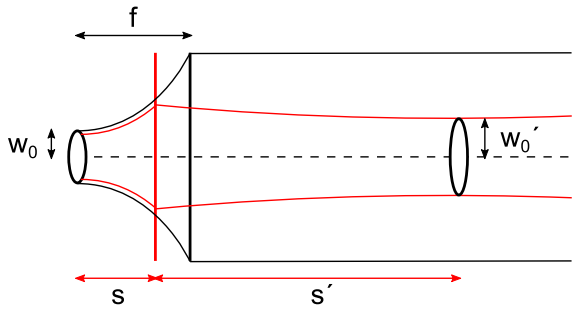

Figure 3.3: *Sketch (not to scale) of optical setup that aligns the beam waist to the cavity. A positive lens collimates the light from the source with waist w_0 when the distance to the source s is equal to the focal distance f (black lines). If s is smaller than f, an image with waist w_0' is formed at a distance s' (red).*

w_0' is calculated from

$$w_0' = \frac{w_0^2}{\left(1 - \frac{s}{f}\right)^2 + \frac{z_R}{f}^2} \tag{3.21}$$

with w_0 the waist of the source, s the distance from the object to the lens, and f the focal length of the lens [35]. For alignment, the relevant information is how far the lens needs to be from the object. Rewriting Equation 3.21 yields

$$s = f - f\sqrt{\frac{w_0^2 - w_0'^2\left(\frac{z_R}{f}\right)^2}{w_0'^2}} \tag{3.22}$$

Finally, one needs to know how far the lens should be from the cavity. The image distance s' is calculated from

$$s' = \left(\frac{1}{f} - \frac{1}{s + \frac{z_R^2}{s-f}}\right)^{-1} \tag{3.23}$$

Here, the parameters are $w_0 = 3.5\,\mu\text{m}$, $w_0' = 200\,\mu\text{m}$, $\lambda = 637\,\text{nm}$, and $f = 11\,\text{mm}$. From Equation 3.22 and 3.23, the object distance s is calculated to be 10.8 mm and the image distance s' is calculated to be 59 cm.

3.2.2 Protocol

The steps in achieving a stable lock with the setup described in Section 3.2.1 are described here.

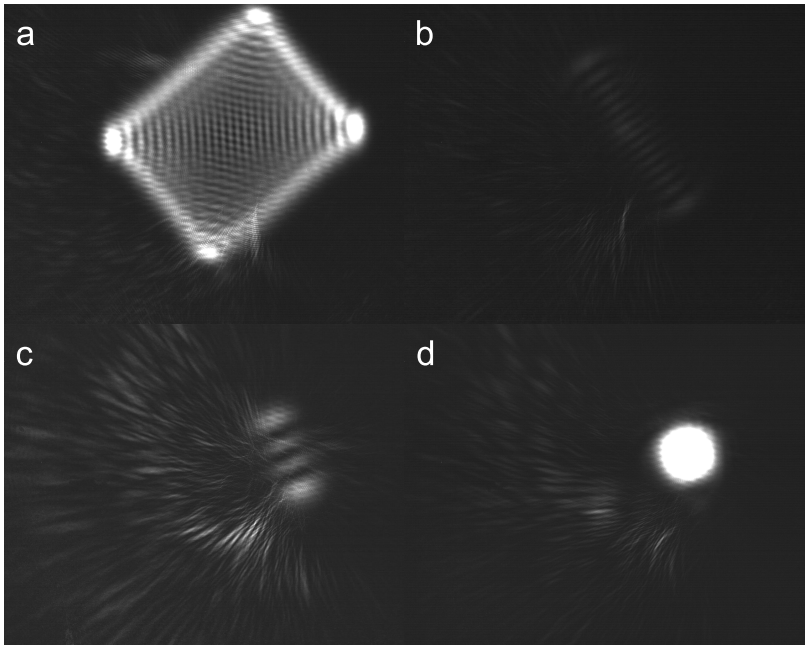

Figure 3.4: *CCD camera images of transmitted light through the cavity at different stages of laser alignment.* ***a****. During initial alignment with a large frequency range.* ***b****. During fine alignment after decreasing the scan range.* ***c****. After tuning the alignment to the lowest possible mode at this frequency.* ***d.*** *Final result at frequency resonant with fundamental cavity mode.*

First, one needs to make sure that the laser beam is well aligned with the fundamental mode of the cavity. Course alignment is carried out by guiding the reflected beam back to its origin. Then, the CCD camera behind the cavity is used to align the beam in such a way that it excites the fundamental cavity mode. Whether any light will be transmitted through the cavity depends on both the frequency and the alignment of the beam. Therefore it is recommended to sweep a large frequency range during the initial alignment. By enabling the voltage scan and setting the scan amplitude to 1 V on the DLC, one makes sure that the frequency being off will not be the reason for seeing no transmission signal on the CCD. As soon as some transmission becomes visible on the CCD, as in Figure 3.4a, the scan amplitude can be decreased to 0.2 V or less and to enable fine align-

ment. At smaller scanning ranges, one first needs to find a frequency that is resonant with the cavity by varying the scan offset on the DLC. Then, the alignment is tuned in order to minimize the number of bright spots on the camera, indicating the excitation of the lowest order mode possible at that frequency. An example of this procedure is shown in Figure 3.4b and 3.4c. When tuning does not decrease the number of bright spots any more, vary the scan offset on the DLC to arrive at a different resonance frequency, and repeat the alignment until one arrives at the fundamental mode, a single spherical spot on the camera (Figure 3.4d).

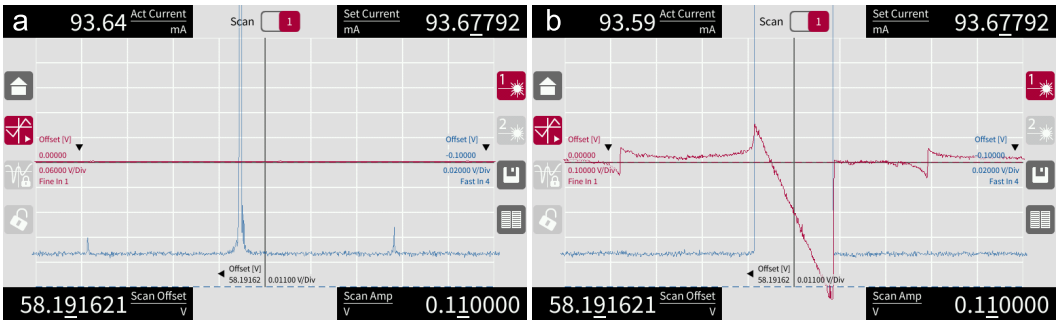

Figure 3.5: *Front panel of the DLC with monitor output of the FALC module in red and transmission signal on the photodiode in blue.* ***a****. After tuning the phase and gain without integral feedback.* ***b****. After enabling and tuning integral feedback.*

After successfully aligning the laser beam to the cavity, the feedback parameters need to be adjusted to allow for locking the laser frequency. For this purpose, the front panel of the DLC with the monitor output of the FALC module and the transmission photodiode signal connected to it will be useful. The feedback is initially switched off with the switch on the FALC module. First, the resonance frequency of the cavity is found by varying the scan offset at a scan amplitude of 0.12 V until the resonance peak shows up on the DLC and a single spot appears on the CCD. The resonance peak and the two sidebands should be visible on the DLC. Now switch on the feedback, but keep the flip switches that control the integral part of the PID at their default position (all switched off, except for the one marked by a circle). Increase the output gain of the FALC module slowly until the feedback curve starts changing, and then tune the phase on the PDH module such that the transmission signal from the photodiode on the DLC shoots up (Figure 3.5a). One might need to vary the parameters of the PDH module a little to get optimal results, but the

combination of PDH phase and FALC gain largely determine the locking behaviour. When proportional feedback has been achieved succesfully, the next step is to enable the integral part. The fifth switch counting from the bottom is flipped, after which it will be necessary to recover the lock by adjusting the offset screw on the FALC module and possibly changing the gain. In general, the addition of the integral part increases the stability strongly. In the end, the feedback and transmission signal should look like Figure 3.5b. For good alignment and parameters, enabling feedback with the FALC module changes the transmission on the camera from Figure 3.6a to Figure 3.6b.

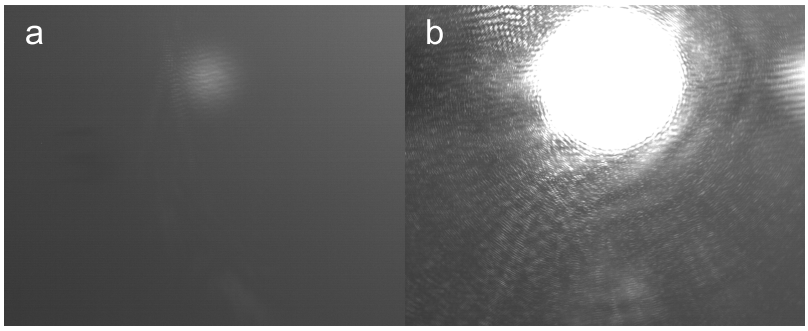

Figure 3.6: *CCD camera image of transmitted light through the cavity* ***a****. without locking and* ***b.*** *with an effective lock*

3.3 Results

In order to characterize the frequency stability of the laser in the Pound-Drever-Hall feedback scheme, a second reference cavity is built to provide feedback for a second laser. By interfering the two lasers on a beamsplitter and observing the beat pattern of the two on a photodiode, the stability of the frequency difference is measured. To understand the sources of frequency fluctuations, each cavity is characterized individually as well. In Figure 3.7, cavity 1 and 2 and laser 1 and 2 are indicated on the optical table.

The main difference between the two cavities is that the spacer between the mirrors in cavity 1 is made of zerodur, whereas the spacer in cavity 2 consists of invar. Zerodur has a thermal expansion coefficient that is about 100 times lower than invar, so cavity 1 is expected to be much more stable against temperature fluctuations. Additionally, cavity 1 is mounted in a way that provides more isolation of vibrations. Where the vacuum tube

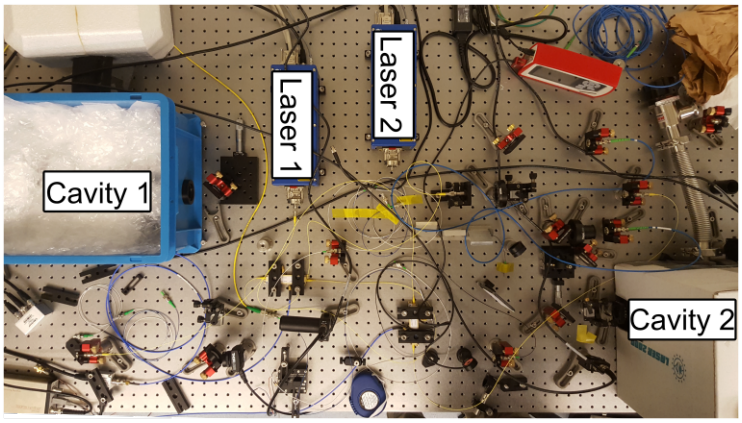

Figure 3.7: *Optical table with cavity 1 and 2 and laser 1 and 2 as referred to in this section.*

of cavity 2 is clamped to the table with only a layer of isolation rubber in between, the vacuum tube of cavity 1 is mounted in a separate box that is loosely connected to the optical table.

3.3.1 Ringdown

In a ringdown measurement, the decay of light out of the cavity after suddenly switching off the light input is used to determine the cavity linewidth. Ringdown measurements were carried out by locking one laser to one cavity, then using an EOM to tune the light into resonance with the other cavity, and then rapidly switching to an off-resonance frequency. The exponential decay of transmitted light is described by

$$I(t) = Ae^{-\frac{t}{\tau}} = Ae^{-2\pi\Delta f t} \tag{3.24}$$

where Δf is the cavity linewidth. Figure 3.8a shows the ringdown measurement of cavity 1, yielding a linewidth of $2.3(1)$ kHz. In Figure 3.8b, the ringdown of cavity 2 is plotted, yielding a linewidth of $2.9(1)$ kHz. Since both cavities have similar mirrors, it is expected that the linewidth of both cavities is similar.

3.3.2 Frequency scan

In order to further characterize both cavities, additional measurements are carried out in a similar fashion to the ringdown experiment. Again, one

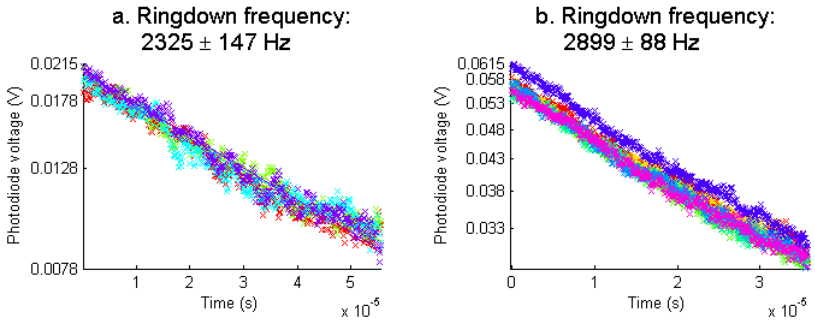

Figure 3.8: *Transmitted light through* ***a.*** *cavity 1 and* ***b.*** *cavity 2 after abruptly changing the frequency away from resonance. By fitting exponential decay to several single-shot measurements, the linewidth of cavity 1 is found to be* $2.3(1)$ kHz *and the linewidth of cavity* $2.9(1)$ kHz*.*

laser is locked to one cavity, and it is tuned to resonance with the other cavity with an EOM. Instead of abruptly changing the frequency of the light going into the cavity under investigation, we now scan the frequency over the resonance while measuring transmission through the cavity. The resulting curve is a convolution of the cavity and laser linewidth. For cavity 1, with the laser locked to cavity 2, the result is shown in Figure 3.9a, and the other way around is plotted in Figure 3.9b.

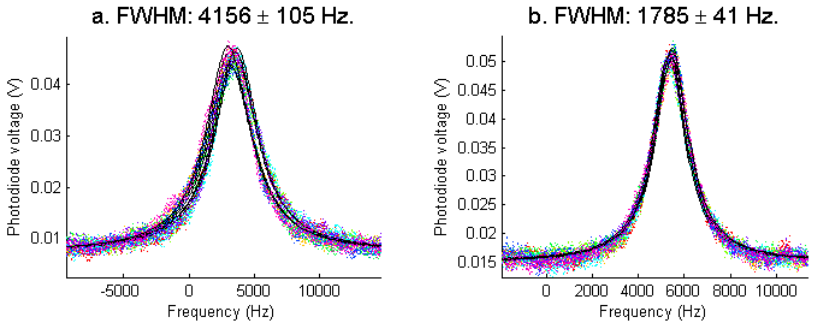

Figure 3.9: *Transmitted light* ***a****. through cavity 1 when scanning the frequency of a laser locked to cavity 2 over resonance at* 205 Hz *and* ***b****. through cavity 2 when scanning the frequency of a laser locked to cavity 1 over resonance at* 202 Hz*. The repetition rates of the frequency scans can neither be too low, because then drift starts to play a role, nor too high, because then one actually measures the field buildup and ringdown in the cavity instead of a linewidth. The black curves show Lorentzian fits to each individual single shot measurement, yielding a linewidth of* $4.1(1)$ kHz *for the convolution of cavity 1 and a laser locked to cavity 2 and* $1.79(4)$ kHz *for the convolution of cavity 2 and locked laser 1.*

3.3.3 Beat measurement

A beat measurement is the most unambiguous measure of laser linewidth. From the width of the beat peak in the frequency domain, the linewidth of the frequency difference between the lasers is obtained. The setup for measuring the beat is shown schematically in Figure 3.10.

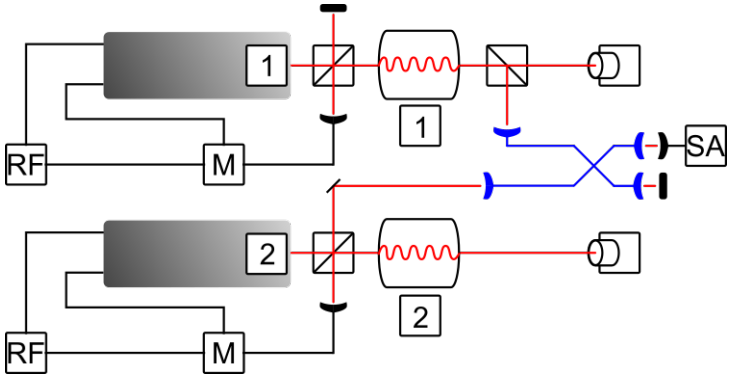

Figure 3.10: *Setup for measuring (the linewidth of) the beating frequency between the two locked lasers. Laser 1 and laser 2 are locked to cavity 1 and 2 respectively as described in Section 3.1.2. The radio frequency (RF) source provides a modulation signal to the laser and to the mixer (M), where it is mixed with the signal of a photodiode measuring the reflection off the cavity to generate an error signal for the laser feedback. For a detailed description of the locking setup, see Figure 3.2. The light of laser 1 transmitted through cavity 1 is overlapped on a beamsplitter with the full spectrum of laser 2 and measured on a photodiode to measure the beating. The photodiode is connected to a spectrum analyzer (SA) to investigate the linewidth of the beat peak.*

Figure 3.11 shows a measured spectrum on the spectrum analyser. In the setup of Figure 3.10, the full spectrum of one locked laser is overlapped with the narrow transmission of the cavity to which the other laser is locked. The convolution therefore reveals the sidebands added to the spectrum of the laser in the PDH scheme as well as the bumps indicating the boundaries of the locking range at around 1 MHz from the central peak. A high resolution scan is necessary to resolve the linewidth of the beat peak, but the fact that the laser locked to cavity 2 drifts by several kilohertz per second complicates such a measurement. In Figure 3.12 the frequency of both locked lasers is plotted as measured on the wavemeter over several minutes.

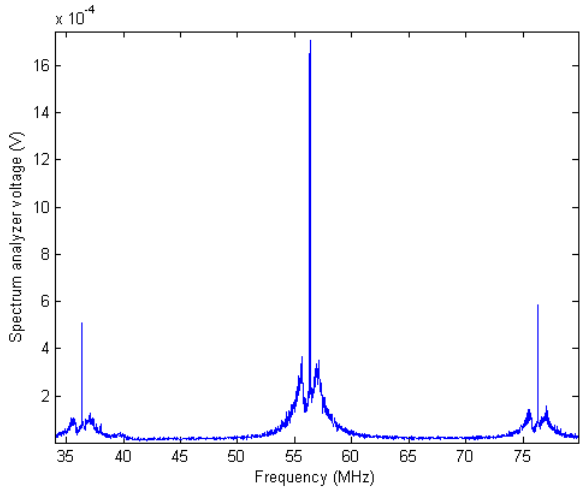

Figure 3.11: *Beat spectrum measured on the spectrum analyzer. The central peak corresponds to the beating frequency of the two lasers. The two peaks at* 20 MHz *above and below this frequency are the frequency sidebands of laser 2 as generated as part of the PDH locking scheme. The bumps around the peaks indicate the locking range or bandwidth of about* 2 MHz*.*

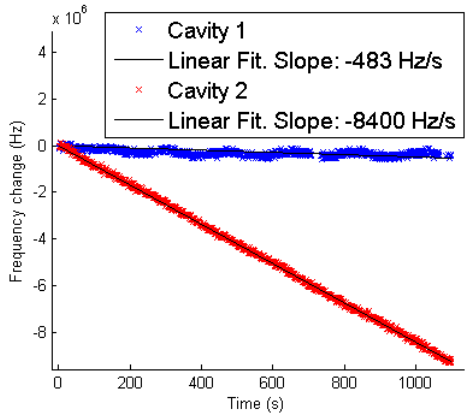

Figure 3.12: *Frequency change of laser 1 locked to cavity 1 (blue curve) and laser 2 locked to cavity 2 (red curve) over 20 minutes as measured with a wavemeter. Measurements were not taken simultaneously. The wavemeter is specified to have an accuracy of* $\pm$ 2 MHz*, so the fluctuations of laser 1 stay well below that value. A linear fit of the frequency drift yields* 0.5 kHz s^{-1} *for cavity 1 and* 8.4 kHz s^{-1} *for cavity 2.*

In order to obtain a linewidth at high resolution, it is necessary to measure several spectra and average because of the low signal to noise ratio at

small frequency steps. However, from Figure 3.12 it is clear that in order to average over several traces, the drift must be taken into account. Therefore an iterative beat measurement is introduced.

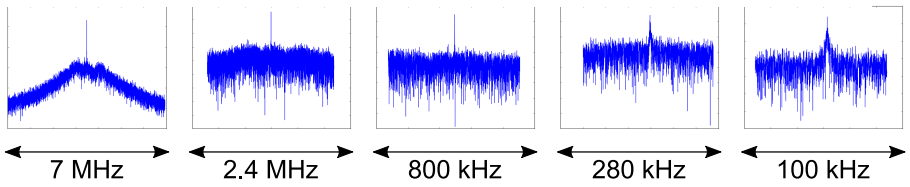

Figure 3.13: *Example of iterative measurement sequence, that detects the frequency of the beat peak and automatically zooms in on the beat frequency while increasing the resolution.*

First, a low-resolution large-range frequency scan is taken, and then the range is decreased step by step while centering around the peak frequency until a high-resolution small-range frequency scan is reached. An example of such a sequence is provided in Figure 3.13. This iterative beat measurement is repeated 15 times. The last iteration of each yields a high resolution frequency scan with an average acquisition time of 73 ms; taking the average results in the beat peak of Figure 3.14, with a fitted FWHM of 5.04(8) kHz. The frequency at the maximum of the individual spectra gives insight in the frequency drift during the acquisition of the 15 measurements. From a linear fit of the frequency at the maxima, the drift is found to be 18.63(3) kHz s^{-1}.

Averaging the final spectra of 15 iterative measurements only works if the frequency drift is identical during each frequency scan. If it is not, the peak drifts slightly more during the acquisition of one spectrum compared to the other, causing the averaged peak to smear out. In order to compensate for this effect, a Lorentzian curve is fitted to each individual experiment, and the spectra are aligned by the center of the Lorentzian before averaging. Figure 3.15 shows all Lorentzian fits. In Figure 3.16 the result of aligning and averaging the 15 spectra is plotted. From the Lorentzian fit of this averaged curve, a linewidth of 3.35(5) kHz is determined. Note that the errors on the values found in Figure 3.8 and 3.9 are derived from several single-shot measurements, thus including fluctuations between measurements, while the errors on the values found in Figure 3.14 and 3.16 are fitting uncertainties and have a purely statistical meaning.

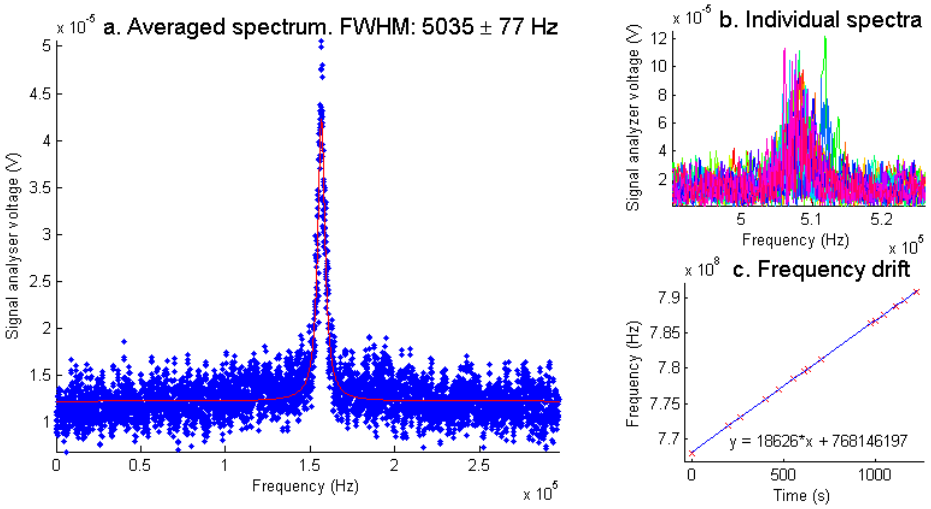

Figure 3.14: *Average of 15 beat peak spectra, obtained by iterative measurements. The Lorentzian fit gives a linewidth of* $5.04(8)$ kHz. *Top inset: noisy individual spectra. Bottom inset: peak frequency in Hertz of individual spectra (red crosses) plotted against time in seconds. The linear fit gives a drift of* $18.63(3)\,\mathrm{kHz\,s^{-1}}$.

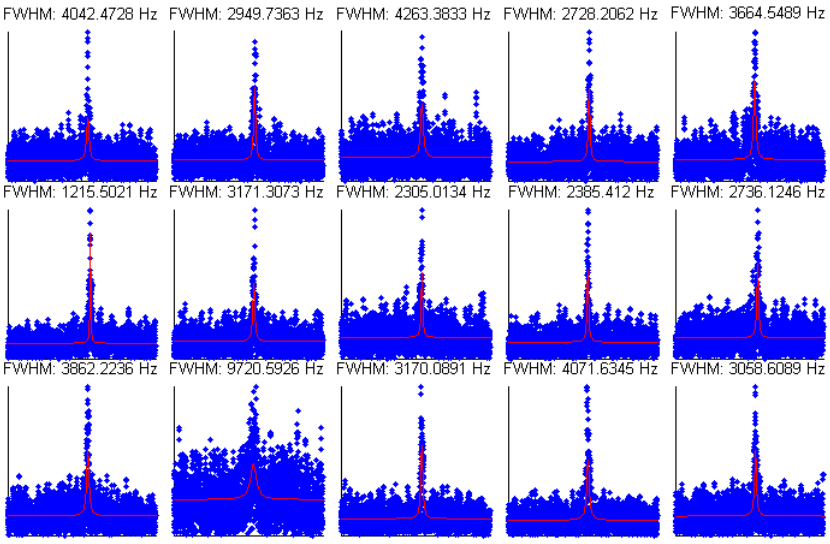

Figure 3.15: *Lorentzian fits of each individual beat peak spectrum. The center of the Lorentzian can be used to align the spectra for averaging.*

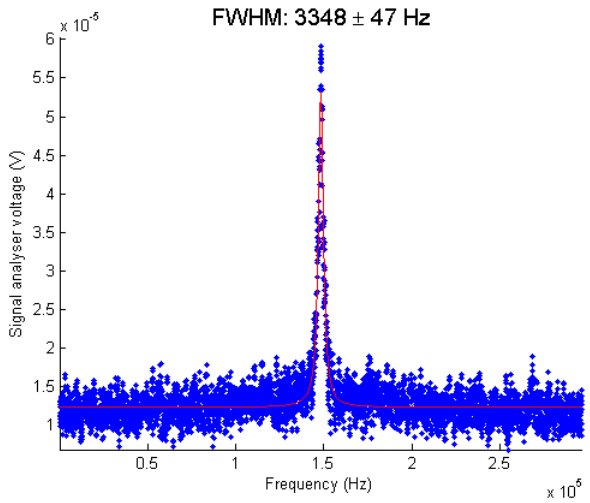

Figure 3.16: *Average of 15 beat peak measurements, aligned by fitting a Lorentzian to the individual spectra as shown in Figure 3.15. From a Lorentzian fit, the linewidth is found to be* 3.35(5) kHz*.*

3.4 Discussion and Conclusion

The ringdown frequency of both cavities gives an expected upper bound on the stability of the individual locked lasers. Due to the steep gradient of the error signal near resonance in the Pound-Drever-Hall scheme, the locked laser linewidth should be smaller than the cavity linewidth. The result of Figure 3.9b is surprising, since the measured linewidth is smaller than the ringdown frequency of cavity 1. One can think of several reasons for a broadened linewidth in the frequency scan compared to the ringdown frequency, as in Figure 3.9a, but we are unable to explain a narrower linewidth.

The result of the beat measurement in Figure 3.16 provides an unambiguous upper bound on the stability of the two laser systems combined. The achieved combined linewidth of 3.35(5) kHz over 73 ms. An upper bound for the linewidth of a single laser is therefore 1.7 kHz. Compared to the required frequency stability of tens of Hertz for entanglement over 10 km with phase stability of 1°, the measured linewidth is too high. Figure 3.17 shows the achieved phase stability for a single laser linewidth of 1.7 kHz as a function of distance. However, one should keep in mind that this is the linewidth in the worst case of both lasers having an equal contribution to the beat peak; from Figure 3.9 it is expected that laser 2 dominates the linewidth. Moreover, the demonstrated stability is measured over tens of

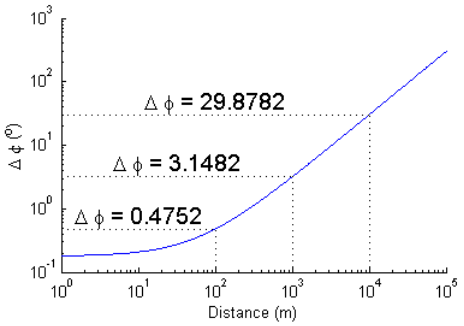

Figure 3.17: *Phase stability as a function of distance for a laser with a linewidth of* 1.7 kHz.

milliseconds, while the required time is on the order of tens of microseconds. It is likely that the short-term stability is higher than the measured beat frequency. Nevertheless, others have achieved more than an order of magnitude higher stability with similar setups [36] [37] [38]. How is it possible that such narrow beat linewidths were not measured here?
The reason for the relatively high linewidth is found in Figure 3.12. The strong frequency drift that was also observed during the beat peak measurement is almost entirely caused by the cavity with the invar spacer. The difference in frequency drift in Figure 3.12 can be explained by the difference in thermal expansion coefficients between zerodur and invar. For invar, a temperature change of 1 mK will cause a frequency change of 1 MHz:

$$\frac{\Delta L}{L_0} = \frac{\Delta f}{f + \Delta f} = \alpha \Delta T \tag{3.25}$$

where $\frac{\Delta L}{L_0}$ is the relative length change, α is the thermal expansion coefficient with an assumed value of $1.6 \times 10^{-6}\,\mathrm{K}^{-1}$ for invar [39], f is the frequency and Δf is the frequency change. This simple calculation proves that without any temperature stabilization, the invar cavity will induce such large frequency drifts that narrow linewidth beat measurements are obstructed. For example, resolving a beat peak with a linewidth of 600 Hz with 10 datapoints would require a measurement time of $10 \times \frac{1}{60\,\mathrm{Hz}} = 167\,\mathrm{ms}$, by which at a frequency drift of $18\,\mathrm{kHz\,s^{-1}}$ the resonance frequency has drifted by 3 kHz. Resolving narrower peaks requires even longer measurement times. It is very well possible that the actual laser linewidth is narrower than the measured value, but that it cannot be resolved in the current measurement setup. Each of the similar setups achieving a narrow linewidth involved temperature stabilization and ultra low

expansion glass instead of invar.
There are several options to improve the linewidth of the stabilized laser. First, one could implement active temperature stabilization. A feedback loop with heating elements should keep the temperature constant to minimize frequency drift. In Reference [36], the vacuum chamber is stabilized at 27 °C with a root-mean-squared fluctuation of less than 1 mK. The thermal expansion coefficient of ultra low expansion glass has an optimum temperature around which the expansion is minimal. Measuring this optimum and adjusting the temperature feedback set point accordingly can reduce the thermal expansion coefficient by an order of magnitude [38]. Additionally, improved mechanical isolation can be achieved by mounting the cavity vertically and enclosing it with a box to shield it from acoustics.

Chapter 4

Conclusion and Outlook

This thesis demonstrates two systems for improved control of the excitation and emission frequencies involved in long distance quantum entanglement with NV centres.
An autonomous monitor-and-solve routine for the frequencies of the readout transition, the spin repump transition and the charge repump transition of the NV centre is presented. By automatic optimization of the excitation frequencies, it is able to keep these frequencies on resonance without human intervention for many hours of experimenting, despite the occurrence of numerous frequency jumps. It allows for the measurement of resonant frequencies as experiments take place, building a large dataset of frequency time series. The frequency jumps in these datasets hint at a bistable process, possibly well-predictable with a machine learning algorithm.
Furthermore, a setup has been built to stabilize a laser to a reference cavity. For characterization of the frequency stability of the locked laser, a second setup with a second cavity that provides feedback for a second laser was implemented as well. The cavities have similar linewidths, $2.3(1)$ kHz and $2.9(1)$ kHz respectively, but the thermal expansion coefficient of the second cavity spacer is a factor 100 higher. As a consequence, a strong drift on the order of tens of kilohertz per second is measured on the frequency of the second laser. The linewidth of the beat peak of the two lasers is found to be $3.35(5)$ kHz. However, due to the drift during this measurement, measuring a narrower linewidth is obstructed. The measured frequency stability would guarantee a phase stability better than 5° over a distance of 1 km. Active temperature stabilization is necessary to obtain a narrower linewidth as required for phase stability in long distance entanglement with NV centres.

The automated optimizer is only a first step towards a fully autonomous quantum node. In a functional quantum network with interconnected NV centres [40], it is undesirable to require a manned control centre at each node. Instead, one would extend the achieved automated control to other parameters of the setup. Concretely, calibration and alignment need to be carried out by software, meaning that all relevant optics should be addressable with different kinds of servos. There is also room for improvement in passive stabilization by shielding the setup better from external fluctuations to minimize the required realignment. In the end, the quantum node containing the NV would be a stand-alone black box that is easily incorporated into a network.
To use this black box in a real long distance network, its functionality should stretch beyond the simple entanglement protocol presented in this thesis. Increasing the rate of entanglement under extreme photon loss will be crucial for any practical application, but it requires more advanced protocols that involve a quantum memory [41]. The NV centre is naturally suited for such protocols, with the nuclear spins of ^{13}C isotopes serving as memory [42], but even higher phase stability will be necessary. A stabilized laser with further improved stability will therefore be a vital part of the quantum node setup.
Finally, when all building blocks (including enhancement of emission into the zero phonon line [43] and downconversion of entangled photons to telecom wavelength [44]) that constitute the outlined stand-alone quantum node have been developed, the only remaining challenge is the distribution and linking up of the nodes to realize a quantum internet.

Appendix A

Appendix

A.1 Auto optimizer parameters

Parameter	Description
overseer	
min_cr_counts	When the babysitter is running, it only activates the *auto_optimizer* when the readout counts per CR check are lower than this value and the counts per repump are lower than *min_repump_counts*. It is recommended to keep this value quite low compared to the counts on resonance, so that the *auto_optimizer* is not running all the time: the PIDs are able to pull the counts up quite a bit, the *auto_optimizer* is only needed to get the counts high enough for the PIDs to work.
min_repump_counts	See *min_cr_counts*.
read_interval	Interval (in seconds) between checks of the babysitter to see if everything is going well or a transition needs to be optimized. If all is on resonance, the frequencies are logged.
stop_optimize	Should in general be false. Stop_optimize is used to directly exit an optimization run from an object other than the *auto_optimizer*. As long as it is True, any optimization run will break before doing anything.

auto_optimizer	
NV0_zeros	In the *auto_optimizer*, the function *check_deionization()* checks whether the NV is in NV^- or NV^0. If the number of zeros in the data stream (see *detect_cycles*) is larger than *NV0_zeros*, the NV is found to be in NV^0, if the number of zeros is smaller than *NV0_zeros*, the NV is found to be in NV^-
check_gate_threshold	If the average readout counts per CR check in the data stream (see *detect_cycles*) is lower than *check_gate_threshold*, the optimizer starts optimizing the gate.
check_yellow_threshold	If the average of the highest 50 % in the data stream (see *detect_cycles*) of the counts per repump is higher than *check_yellow_threshold*, the charge rempump laser is resonant. If there are also zeros on the counts per repump datastream, the spin repump laser might still be off resonance.
check_newfocus_zeros	If there are both high values and zeros on the counts per repump data stream (see *detect_cycles*), the charge repump laser is resonant while the spin repump laser is not. If the number of zeros in the data stream is larger than *check_newfocus_zeros*, the spin repump frequency is optimized.
data_time	Time between taking data points in the data stream (see *detect_cycles*) and during optimization.
detect_cycles	The decision whether one of the lasers is off resonance cannot be made based on a single data point. Therefore in each check a data stream of *detect_cycles* datapoints, at intervals *data_time* is acquired.

flow_sleep	After an optimization of any frequency has been carried out, the flowchart waits for a moment to move any laser to the new frequency. The waiting time in seconds is *flow_sleep*.
max_gate_iterations	During one cycle of the flowchart of Figure 2.2, the readout transition is optimized at most *max_gate_iterations* times
max_nf_iterations	See *max_gate_iterations* (for the spin repump laser).
max_yellow_iterations	See *min_cr_counts* (for the charge repump laser).
opt_gate_dwell	During the optimization of the readout transition, the optimizer dwells at one frequency while measuring counts per CR check for *opt_gate_dwell* seconds.
opt_gate_good	If at any point during the optimization of the readout transition the counts are higher than *opt_gate_good*, the scan is immediately halted at that frequency.
opt_gate_scan_min	Lowest value from the starting frequency of the readout transition that is visited during the optimization scan.
opt_gate_scan_max	Highest value from the starting frequency of the readout transition that is visited during the optimizations can.
opt_gate_step	Steps by which the frequency is changed during a scan.
opt_yellow_dwell	See *opt_gate_dwell* (for the charge repump laser)
opt_yellow_good	See *opt_gate_good* (for the charge repump laser)
opt_yellow_scan_min	See *opt_gate_scan_min* (for the charge repump laser)
opt_yellow_scan_max	See *opt_gate_scan_max* (for the charge repump laser)
opt_yellow_step	See *opt_gate_step* (for the charge repump laser)
opt_nf_dwell	See *opt_gate_dwell* (for the spin repump laser)

opt_nf_good	See *opt_gate_good* (for the spin repump laser)
opt_nf_scan_min	See *opt_gate_scan_min* (for the spin repump laser)
opt_nf_scan_max	See *opt_gate_scan_max* (for the spin repump laser)
opt_nf_step	See *opt_gate_step* (for the spin repump laser)
yellow_delay	There seems to be a delay in the readout of the charge repump frequency. This delay has the result that when a high number of counts per repump is detected at a certain optimal frequency, the found frequency is not really optimal, but the actual optimal frequency was reported somewhat later. *yellow_delay* solves this problem partly by waiting *yellow_delay* seconds when the optimal frequency is found and only then exiting the scan. The same delay is present when the threshold for yellow was not exceeded and the frequency with the highest counts of the scan is set: not the frequency at the highest counts needs to be taken, but the frequency *yellow_delay* seconds later.

A.2 Emission simulation

A.2.1 Two photon emission

In the entanglement protocol of Section 3.1.1, the excitation of the $|0\rangle$ state to the $|e\rangle$ state is assumed to be immediate. However, the implementation of the excitation pulse in a real experiment involves excitation pulses of a finite time, allowing for spontaneous emission of a photon even during the pulse. Emission of a photon during the excitation pulse will always destroy entanglement, since it projects the superposition $|0\rangle + |1\rangle$ to the $|0\rangle$ state as soon as the photon is detected. Clearly, experiments in which a photon is detected during the laser pulse should be discarded. A more serious issue emerges when a photon is emitted during and after the excitation pulse, but the first photon is only detected by the environment and

not by a photodetector. In this case successful entanglement might be assumed, since the measurement of the second photon confirms spin-photon entanglement, while the first photon has destroyed the initial superposition and thereby entanglement. The entanglement fidelity will be affected.

Simulation

The probability of two-photon emission is calculated by quantum jump simulation [45]. This Monte Carlo approach simulates individual experiments, which can have sudden jumps in the quantum state due to measurements, and predicts the outcome of a real experiment by averaging many simulated individual experiments. In each individual experiment, laser excitation drives a Rabi oscillation of the population in the excited state ρ_{ee}:

$$\rho_{ee}(t) = \frac{\omega_{Rabi}^2}{(\omega_0 - \omega)^2 + \omega_{Rabi}^2} \sin^2(\frac{1}{2}\sqrt{(\omega_0 - \omega)^2 + \omega_{Rabi}^2}t)$$

where ω_{Rabi} is the Rabi frequency, ω is the laser frequency and ω_0 is the resonance frequency of the excitation. At the same time, spontaneous emission might occur, described by

$$\frac{d\rho_{ee}(t)}{dt} = \frac{2\rho_{ee}(t)}{\tau}$$

where τ is the lifetime of the excited state. The probability of two photon emission can be then be calculated from

$$p_2 = P(\text{photon after pulse} \mid \text{photon during pulse}) * P(\text{photon during pulse})$$

The conditional probability $P(\text{photon after pulse} \mid \text{photon during pulse})$ is the average ρ_{ee} in only the experiments in which a photon was emitted during the pulse experiments, whereas $P(\text{photon during pulse})$ is the fraction of experiments in which a photon was emitted during the pulse. However, in the end this two photon emission is not what determines the infidelity. Since entanglement is assumed only if a photon is detected after the laser pulse, the conditional probability of photon emission during the laser pulse given photon emission after the laser pulse is more important. It can be calculated from Bayes' formula

$$p = P(A \mid B) = \frac{P(B \mid A)P(A)}{P(B)}$$

where in this case A stands for photon emission during the pulse and B for photon emission after the pulse.
Ideally, the entangled state after the entanglement protocol is

$$|\Psi^+\rangle = \frac{1}{\sqrt{2}}(|01\rangle + |10\rangle)$$

When photon emission during the laser pulse is taken into account, it can be described by the density matrix

$$\rho = (1-2p)|\Psi^+\rangle\langle\Psi^+| + p|01\rangle\langle 01| + p|10\rangle\langle 10|$$

The fidelity of $|\Psi^+\rangle$ becomes

$$\begin{aligned}\mathcal{F} &= \sqrt{\langle\Psi^+|\rho|\Psi^+\rangle} \\ &= \sqrt{(1-2p) + \frac{1}{2}p + \frac{1}{2}p} \\ &= \sqrt{1-p}\end{aligned}$$

Results

In order to simulate how the probability of two photon emission depends on the pulse duration in a real experiment, the power of the pulse is varied to maximize ρ_{ee} at the end of the pulse for each duration. Simulations for several pulse durations (and corresponding pulse powers) are plotted in Figure A.1. Results for both the total two-photon probability and the conditional probability of emitting a photon during the pulse given that a photon was emitted after the pulse are plotted in Figure A.2.
Figure A.2 directly relates the pulse duration to infidelity. From analysis of experimental data, the FWHM of the Gaussian laser pulse that is currently used is found to be 3.4 ns. According to Figure A.2, this corresponds to a conditional probability of 11.5 %, resulting in 94.1 % fidelity. Employing a faster arbitrary waveform generator to reduce the pulse duration to 1.0 ns, provided that the electro-optical modulator can handle this, would yield a conditional probability of 3.4 %, leading to 98.3 % fidelity. Therefore decreasing the duration of the excitation pulse is a viable and effective way to increase the entanglement fidelity.

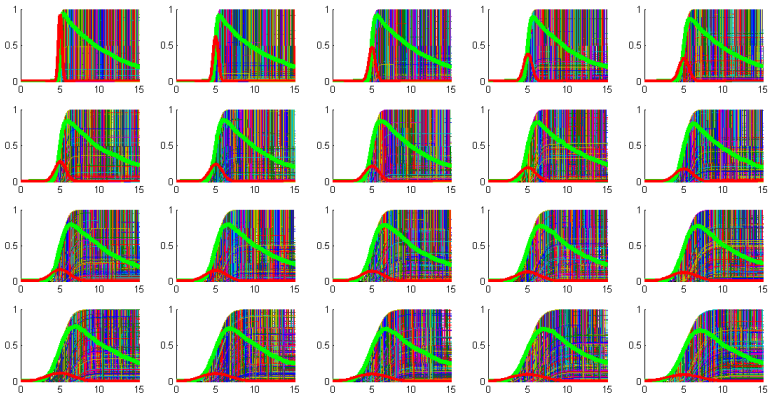

Figure A.1: *Quantum jump simulations of excitation by a Gaussian laser pulse of varying duration. Population in the excited state ρ_{ee} is on the y-axis, time in nanoseconds on the x-axis. The thick green line shows the average ρ_{ee} of all individual experiments, the thick red line shows the laser pulse (with arbitrary y-axis).*

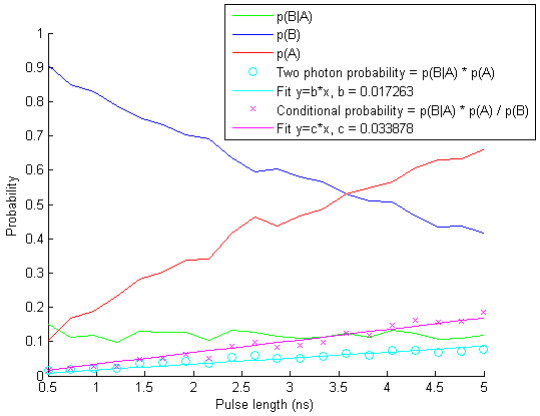

Figure A.2: *Total probability of two photon emission (cyan) and conditional probability (magenta) of emission of a photon during the laser pulse, given that a photon was detected after the laser pulse, as a function of the laser pulse duration. Solid lines plot a linear fit.*

A.2.2 Off-resonant transitions

So far, only the excitation from the $|0\rangle$ to the $|e\rangle$ state has been considered, but excitation of $|1\rangle$ is possible as well. The probability of this transition is strongly suppressed because the laser frequency is resonant with the exci-

tation of $|0\rangle$ to $|e\rangle$; it is detuned with the excitation of $|1\rangle$ by approximately 3 GHz. In principle, photons emitted from this excitation could be filtered because of their different frequency, but in practice such narrow linewidth filters are not available. Again, the probability of exciting the $|1\rangle$ state and emitting a photon is calculated by quantum jump simulation discussed in Section A.2.1. Now the pulse length and pulse power are fixed such that the probability of excitation of $|0\rangle$ to $|1\rangle$ is maximized. The detuning of $|1\rangle$ excitation is varied. Figure A.3 plots the result for the number of emitted photons from the excited state of $|1\rangle$ in 10000 individual quantum jump experiments. The number of photons is expected to be a Lorentzian with a FWHM given by the relation between the FWHM of the excitation pulse and that of its Fourier transform:

$$\mathrm{FWHM}_f = \frac{4\ln(2)}{\pi \mathrm{FWHM}_t}$$

For a detuning of exactly 3 GHz, the fit predicts an off-resonant excitation probability of 0.00077.

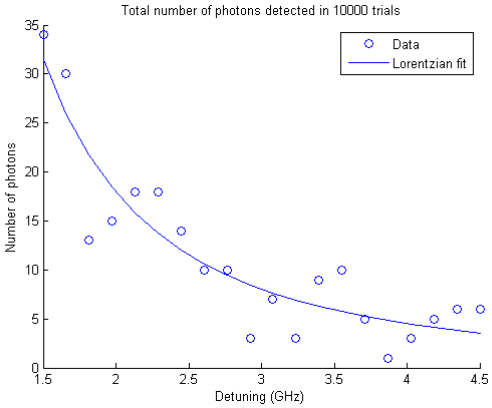

Figure A.3: *Number of photons emitted from off-resonant excitation of $|1\rangle$ by a Gaussian laser pulse with a FWHM of 2 ns in 10000 individual quantum jump experiments. The pulse power is optimized for excitation of $|0\rangle$ to $|e\rangle$. A Lorenztian fit with a fixed FWHM is plotted as a solid curve.*

Acknowledgements

I'm very grateful for the supervision I received from Norbert Kalb and dr. Andreas Reiserer. Norbert, thank you for the time you devoted to our discussions, answering my questions, and checking my manuscript. I'm always impressed by how much you know about the different aspects of the experiment: optics, electronics, programming, theory... Andreas, thank you for introducing me to lasers and cavities - I could not have had a better teacher in building my first optical setup. I thank Prof. dr. ir. Ronald Hanson for letting me be part of his group. Ronald, thank you for having me work on this project that allowed me to develop new skills in a field where I didn't have any experience. Thank you for taking the time to give me comments and share your ideas about my project. Prof. dr. ir. Tjerk Oosterkamp, thank you for being my supervisor from Leiden. I'd also like to thank dr. Peter Humphreys for his helpful comments.
I have learned a lot and really enjoyed my time as well. For that I'd like to thank the whole diamond team and my fellow students in the master room - I've had six great months! I hope that my future will be in a group that is as inspiring and supportive as this group is. Many thanks to Martijn Oei for helpful discussions throughout the project. Finally, I'm grateful to Marianne, and my family and friends for their support during all stages of the project.

Bibliography

[1] I. M. Georgescu, S. Ashhab, and F. Nori, *Quantum simulation*, Reviews of Modern Physics **86**, 153 (2014).

[2] A. A. Houck, H. E. Türeci, and J. Koch, *On-chip quantum simulation with superconducting circuits*, Nature Physics **8**, 292 (2012).

[3] T. D. Ladd, F. Jelezko, R. Laflamme, Y. Nakamura, C. Monroe, and J. L. O'Brien, *Quantum computers*, Nature **464**, 45 (2010).

[4] C. H. Brassard and G. Bennett, *Quantum cryptography: Public key distribution and coin tossing*, Proceedings of IEEE International Conference on Computers, Systems and Signal Processing (1984).

[5] V. Giovannetti, S. Lloyd, and L. Maccone, *Quantum-enhanced measurements: beating the standard quantum limit.*, Science **306**, 1330 (2004).

[6] C. Monroe and J. Kim, *Scaling the ion trap quantum processor.*, Science (New York, N.Y.) **339**, 1164 (2013).

[7] H. J. Kimble, *The quantum internet.*, Nature **453**, 1023 (2008).

[8] N. Brunner, D. Cavalcanti, S. Pironio, V. Scarani, and S. Wehner, *Bell nonlocality*, Reviews of Modern Physics **86**, 419 (2014).

[9] C. H. Bennett, G. Brassard, R. Jozsa, A. Peres, and W. K. Wootters, *Teleporting an Unkown Quantum State via Dual Classical and {EPR} Channels*, Physical Review Letters **70**, 1895 (1993).

[10] L. Childress and R. Hanson, *Diamond NV centers for quantum computing and quantum networks*, MRS Bulletin **38**, 134 (2013).

[11] D. D. Awschalom, R. Epstein, and R. Hanson, *The diamond age of spintronics.*, Scientific American **297**, 84 (2007).

[12] L. Robledo, L. Childress, H. Bernien, B. Hensen, P. F. Alkemade, and R. Hanson, *High-fidelity projective read-out of a solid-state spin quantum register*, Nature **477**, 574 (2011).

[13] T. H. Taminiau, J. J. T. Wagenaar, T. Van Der Sar, F. Jelezko, V. V. Dobrovitski, and R. Hanson, *Detection and control of individual nuclear spins using a weakly coupled electron spin*, Physical Review Letters **109**, 1 (2012).

[14] P. C. Maurer, G. Kucsko, C. Latta, L. Jiang, N. Y. Yao, S. D. Bennett, F. Pastawski, D. Hunger, N. Chisholm, M. Markham, D. J. Twitchen, J. I. Cirac, and M. D. Lukin, *Room-temperature quantum bit memory exceeding one second.*, Science **336**, 1283 (2012).

[15] B. Hensen, H. Bernien, A. E. Dréau, A. Reiserer, N. Kalb, M. S. Blok, J. Ruitenberg, R. F. L. Vermeulen, R. N. Schouten, C. Abellán, W. Amaya, V. Pruneri, M. W. Mitchell, M. Markham, D. J. Twitchen, D. Elkouss, S. Wehner, T. H. Taminiau, and R. Hanson, *Loophole-free Bell inequality violation using electron spins separated by 1.3 kilometres*, Nature **526**, 682 (2015).

[16] C. H. Bennett, G. Brassard, S. Popescu, B. Schumacher, J. a. Smolin, and W. K. Wootters, *Purification of Noisy Entanglement and Faithful Teleportation via Noisy Channels*, Physical Review Letters **76**, 722 (1996).

[17] H.-J. Briegel, W. Dür, J. I. Cirac, and P. Zoller, *Quantum Repeaters: The Role of Imperfect Local Operations in Quantum Communication*, Physical Review Letters **81**, 5932 (1998).

[18] M. Zukowski, A. Zeilinger, M. A. Horne, and A. K. Ekert, *"Event-ready-detectors" Bell experiment via entanglement swapping*, Physical Review Letters **71**, 4287 (1993).

[19] S. Muralidharan, L. Li, J. Kim, N. Lütkenhaus, M. D. Lukin, and L. Jiang, *Efficient long distance quantum communication*, Scientific Reports , 1 (2015).

[20] F. Jelezko and J. Wrachtrup, *Single defect centres in diamond: A review*, Physica Status Solidi (A) Applications and Materials Science **203**, 3207 (2006).

[21] M. W. Doherty, N. B. Manson, P. Delaney, F. Jelezko, J. Wrachtrup, and L. C. L. Hollenberg, *The nitrogen-vacancy colour centre in diamond*, Physics Reports **528**, 1 (2013).

[22] P. Siyushev, H. Pinto, M. Voros, A. Gali, F. Jelezko, and J. Wrachtrup, *Optically controlled switching of the charge state of a single nitrogen-vacancy center in diamond at cryogenic temperatures*, Physical Review Letters **110**, 1 (2013).

[23] K. Beha, A. Batalov, N. B. Manson, R. Bratschitsch, and A. Leitenstorfer, *Optimum photoluminescence excitation and recharging cycle of single nitrogen-vacancy centers in ultrapure diamond*, Physical Review Letters **109**, 1 (2012).

[24] V. Acosta and P. Hemmer, *Nitrogen-vacancy centers: Physics and applications*, MRS Bulletin **38**, 127 (2013).

[25] M. L. Goldman, A. Sipahigil, M. W. Doherty, N. Y. Yao, S. D. Bennett, M. Markham, D. J. Twitchen, N. B. Manson, A. Kubanek, and M. D. Lukin, *Phonon-induced population dynamics and intersystem crossing in nitrogen-vacancy centers*, Physical Review Letters **114**, 1 (2015).

[26] L. M. K. Vandersypen and I. L. Chuang, *NMR techniques for quantum control and computation*, Reviews of Modern Physics **76**, 1037 (2004).

[27] K. H. A. K. H. Ang, G. Chong, and Y. L. Y. Li, *PID control system analysis, design, and technology*, IEEE Transactions on Control Systems Technology **13**, 559 (2005).

[28] R. J. Frank, N. Davey, and S. P. Hunt, *Time Series Prediction and Neural Networks*, Journal of Intelligent and Robotic Systems **31**, 91 (2001).

[29] S. D. Barrett and P. Kok, *Efficient high-fidelity quantum computation using matter qubits and linear optics*, Physical Review A **71**, 060310 (2005).

[30] C. Hong, Z. Ou, and L. Mandel, *Measurement of Subpicosecond Time Intervals between Two Photons by Interference*, Physical Review Letters **59**, 2610 (1987).

[31] H. Bernien, B. Hensen, W. Pfaff, G. Koolstra, M. S. Blok, L. Robledo, T. H. Taminiau, M. Markham, D. J. Twitchen, L. Childress, and R. Hanson, *Heralded entanglement between solid-state qubits separated by three metres*, Nature **497**, 86 (2013).

[32] R. W. P. Drever, J. L. Hall, F. V. Kowalski, J. Hough, G. M. Ford, A. J. Munley, and H. Ward, *Laser phase and frequency stabilization using an optical resonator*, Applied Physics B **31**, 97 (1983).

[33] E. D. Black, *An introduction to Pound–Drever–Hall laser frequency stabilization*, American Journal of Physics **69**, 79 (2001).

[34] K. Predehl, G. Grosche, S. M. F. Raupach, S. Droste, O. Terra, J. Alnis, T. Legero, T. W. Hänsch, T. Udem, R. Holzwarth, and H. Schnatz, *A 920-Kilometer Optical Fiber Link for Frequency Metrology at the 19th Decimal Place*, Science **336**, 441 (2012).

[35] S. A. Self, *Focusing of spherical Gaussian beams.*, Applied optics **22**, 658 (1983).

[36] Y. N. Zhao, J. Zhang, J. Stuhler, G. Schuricht, F. Lison, Z. H. Lu, and L. J. Wang, *Sub-Hertz frequency stabilization of a commercial diode laser*, Optics Communications **283**, 4696 (2010).

[37] G. Kirchmair, *Frequency stabilization of a Titanium-Sapphire laser for precision spectroscopy on Calcium ions*, PhD thesis, Leopold Franzens University of Innsbruck, 2006.

[38] C. Hempel, *Digital quantum simulation , Schroedinger cat state spectroscopy and setting up a linear ion trap*, PhD thesis, Leopold-Franzens University of Innsbruck, 2014.

[39] W. D. Callister, *Materials Science and Engineering. An Introduction*, John Wiley & Sons, Inc., seventh ed edition, 2007.

[40] N. H. Nickerson, J. F. Fitzsimons, and S. C. Benjamin, *Freely scalable quantum technologies using cells of 5-to-50 qubits with very lossy and noisy photonic links*, Physical Review X **4**, 1 (2014).

[41] E. T. Campbell and S. C. Benjamin, *Measurement-based entanglement under conditions of extreme photon loss*, Physical Review Letters **101**, 16 (2008).

[42] A. Reiserer, N. Kalb, M. S. Blok, K. J. Van Bemmelen, T. H. Taminiau, and R. Hanson, *Robust Quantum-Network Memory Using Decoherence-Protected Subspaces of Nuclear Spins*, Physical Review X **6**, 021040 (2016).

[43] R. Albrecht, A. Bommer, C. Deutsch, J. Reichel, and C. Becher, *Coupling of a single N-V center in diamond to a fiber-based microcavity*, in *2013 Conference on Lasers and Electro-Optics Europe and International Quantum Electronics Conference, CLEO/Europe-IQEC 2013*, volume 243602, pages 1–5, 2013.

[44] S. Zaske, A. Lenhard, C. A. Kessler, J. Kettler, C. Hepp, C. Arend, R. Albrecht, W. M. Schulz, M. Jetter, P. Michler, and C. Becher, *Visible-to-telecom quantum frequency conversion of light from a single quantum emitter*, Physical Review Letters **109**, 1 (2012).

[45] M. B. Plenio and P. L. Knight, *The quantum-jump approach to dissipative dynamics in quantum optics*, Reviews of Modern Physics **70**, 101 (1998).